

GLUE: Generative Latent Unification of Expertise-Informed Engineering Models

Tim Aebersold^{a,*}, Sohey Massoudi^a, Mark D. Fuge^a

^aDepartment of Mechanical and Process Engineering, ETH Zurich, Tannenstrasse 3, 8092, Zurich, Switzerland

Abstract

Engineering complex systems (aircraft, buildings, vehicles) requires accounting for geometric and performance couplings across subsystems. As generative models proliferate for specialized domains (wings, structures, engines), a key research gap is how to coordinate frozen, pre-trained submodels to generate full-system designs that are feasible, diverse, and high-performing. We introduce Generative Latent Unification of Expertise-Informed Engineering Models (GLUE), which orchestrates pre-trained, frozen subsystem generators while enforcing system-level feasibility, optimality, and diversity. We propose and benchmark (i) data-driven GLUE models trained on pre-generated system-level designs and (ii) a data-free GLUE model trained online on a differentiable geometry layer. On a UAV design problem with five coupling constraints, we find that data-driven approaches yield diverse, high-performing designs but require large datasets to satisfy constraints reliably. The *data-free* approach is competitive with Bayesian optimization and gradient-based optimization in performance and feasibility while training a full generative model in only ~ 10 min on a RTX 4090 GPU, requiring more than two orders of magnitude fewer geometry evaluations and FLOPs than the data-driven method. Ablations focused on *data-free* training show that subsystem output continuity affects coordination, and equality constraints can trigger mode collapse unless mitigated. By integrating unmodified, domain-informed submodels into a modular generative workflow, this work provides a viable path for scaling generative design to complex, real-world engineering systems.

Keywords: Generative Design, Multidisciplinary Design Optimization, Artificial Intelligence, Machine Learning, Latent Space, UAV

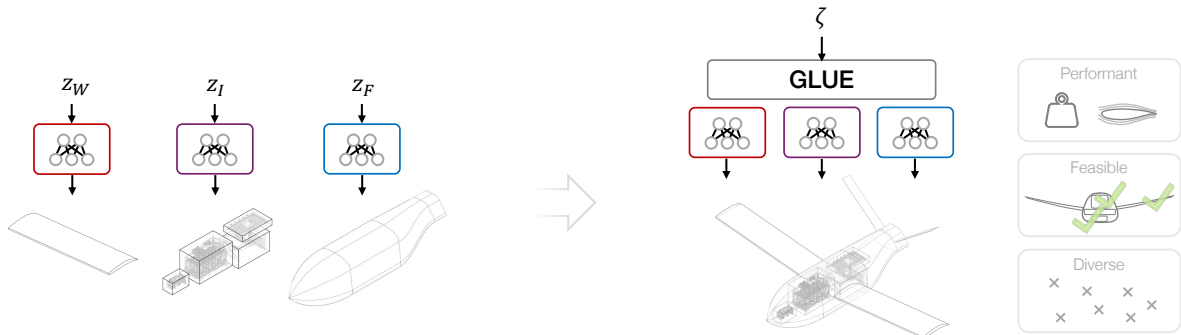


Figure 1: **Given:** Frozen, pre-trained specialized models with latents z_i . **Contribution:** Coordination with GLUE models from system-level latent ζ .

1. Introduction

Generative models have been applied to engineering design problems ranging from architecture [1] to aerospace [2] and drug discovery [3]. Once trained, fast inference allows them to support design-space exploration and decision-making in ways that are difficult to match with traditional optimization algorithms alone [4]. Many such models compress designs into

interpretable, low-dimensional latent spaces (z), which makes high-dimensional trade spaces more tractable.

In practice, these generative models are almost always purpose-trained for a specific domain and often for a single component (*e.g.*, a wing, fuselage, or structural part). Domain-informed priors in the parametrization, architecture, and loss typically improve performance and validity on that narrow task. Yet real-world engineering problems (*e.g.*, an aircraft) are inherently multi-component and multi-domain. This necessitates accounting for coupled interfaces, constraints, and objectives across subsystems. The system optimum rarely equals the sum of subsystems optimized in isolation.

*Corresponding author

Email addresses: taebersold@ethz.ch (Tim Aebersold), smaassoudi@ethz.ch (Sohey Massoudi), mafuge@ethz.ch (Mark D. Fuge)

Current approaches to multi-component systems largely rely on generative models trained end-to-end for the entire system, which enforces a single architecture and loss formulation. This makes it difficult to distribute work across teams or incorporate pre-trained third-party models. As generative modeling is applied to increasingly complex real-world engineering systems, we inevitably need methods to combine several pre-trained, specialized generative models (see Figure 1). To preserve their validity or any certifications or bounds provided by the original subsystem model creators, the pre-trained subsystem models ideally remain frozen. The critical gap is thus a coordination mechanism that operates on *pre-trained* domain-informed subsystem models *without modification*. It should expose a system-level latent ζ that offers a low-dimensional, human-interpretable space for system-level design exploration and synthesize designs that satisfy three key criteria:

- *Exact feasibility*: Satisfy all coupling constraints and system-level requirements precisely.
- *System-level optimality*: Optimize performance objectives across the entire system.
- *Diversity*: Generate varied designs across the feasible design space.

Key Contributions. To address this coordination challenge, we make the following contributions.

1. We introduce GLUE models, which orchestrate pre-trained, frozen generative models across subsystems, exposing a low-dimensional system-level latent space ζ . We propose and compare two training paradigms:
 - *Data-Driven (DD)* GLUE models train on feasible, high-performing designs generated by conventional optimization algorithms.
 - *Data-Free (DF)* GLUE models learn orchestration directly by backpropagating gradients from a differentiable, parallelizable geometry layer.
2. We benchmark both paradigms on a multi-component Unmanned Aerial Vehicle (UAV) design problem, demonstrating that DF-GLUE:
 - a) Achieves over two orders of magnitude greater computational efficiency than DD-GLUE.
 - b) Is near-competitive with gradient-based and Bayesian optimization in optimality and feasibility while being more robust to local minima.
 - c) Enables explicit, user-controlled trade-offs between diversity and optimality.
3. We ablate DF-GLUE to identify the key factors enabling effective coordination, such as subsystem model quality and handling of equality constraints.

2. Related Work

We provide (i) a brief introduction to generative modeling for engineering design, including UAVs. We (ii) draw parallels

between the architectures used in Multidisciplinary Design Optimization (MDO) and the current state of generative modelling for multi-domain systems, and (iii) examine training strategies that target feasible, performant, and diverse designs in generative models for engineering.

2.1. Generative Models for Engineering Design

Machine learning models for engineering and science have been applied to problems ranging from airfoil generation [2] and composite beam structures [5] to photonics [6], inverse drug and molecular design [7, 3], architectural layout modeling [1] and more. We distinguish between two uses of models. *Neural surrogate models* predict performance from geometry, replacing costly simulations with near-instant evaluation [8, 9, 10, 11] and have been extensively applied to MDO [12, 13, 14, 15]. However, surrogates lack two key advantages of generative models: (i) fast inverse design to explore trade spaces and (ii) a structured, interpretable, low-dimensional latent space. In this paper, we focus solely on *generative models*, which directly create novel geometries based on random noise, performance requirements or user-specified conditions.

In engineering, design problems are usually high-dimensional (*i.e.*, a design is described by a large number of variables). Generative Adversarial Networks (GANs) [16] and Variational Autoencoders (VAEs) [17] applied extensively in engineering [2, 18, 19] and address this by compressing design features into interpretable, low-dimensional latent spaces. For VAEs and GANs, [20] and [21] introduce methods to disentangle these latent spaces to create interpretable principal axes, which enables human exploration and decision-making. Optimal transport GANs [22, 23, 24] have been proposed to address the shortcomings of unstable adversarial training. More recently, diffusion models [25, 26] have shown promising results in topology optimization, flow surrogates, and airfoil generation [27, 28, 29, 30, 31]. For an overview of further model architectures and applications to engineering, we refer to [19]. We build on these prior contributions, both for our subsystem generators (Section 3.2, Appendix B) and for the data-driven GLUE variants we evaluate (Section 3.5).

2.2. Multidisciplinary Design Optimization

Extending generative modeling to multi-component systems places our work within the scope of MDO, originally popularized by Cramer *et al.* [32] and Sobiesczanski-Sobieski [33]. Rooted in aircraft design, MDO coordinates coupled disciplines so components are co-optimized rather than tuned in isolation. MDO has been applied across many domains [34], including UAV design [35, 36].

2.2.1. Monolithic and Distributed MDO

Martins and Lambe [34] contrast *monolithic* MDO (all design variables optimized within a single framework) with *distributed* MDO (decomposition into discipline-level subproblems with explicit or implicit coordination). We use this distinction to draw direct parallels for generative models.

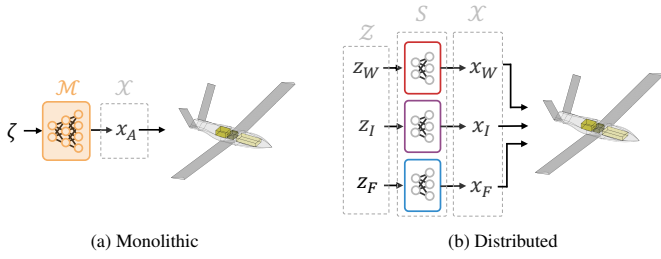


Figure 2: Monolithic and distributed generative modeling. Approach (b) enables specialized models but requires latent coordination.

2.3. Monolithic and Distributed Generative Modeling

We interpret this analogy as follows (see Figure 2). A *monolithic generative model* is a *single* model trained on the full design space across all disciplines and components. For example, Cobb *et al.* [18] train a single VAE for an entire race car. So far, for multi-component systems, the overwhelming focus has been on this approach [37, 38].

In contrast, the *distributed* generative approach employs *multiple* generative models for individual subsystems or disciplines, then coordinates between them. Many existing models can be interpreted as subsystem models (S in Figure 2). Examples include models for airfoils and wings [2, 29], and structural components [27, 39]. The distributed approach offers two major advantages:

1. *Domain-Specific Priors and Architectures.* Felten *et al.* found that “[...] domain-informed generative models improve performance” [40], consistent with many specialized models that embed domain knowledge in architectures, losses, or parametrization [2, 29, 39]. Distributed modeling allows one to retain domain-informed tweaks for each submodel. In contrast, monolithic generative approaches are tied to a single architecture and loss formulation, which is especially restrictive when subsystems require different modeling approaches.
2. *Organizational Advantages.* Industrial practice typically distributes design tasks to specialized engineering groups that retain control over their procedures and in-house expertise rather than deferring to a central authority, a pattern emphasized in MDO literature by Kroo [41] and Martins [34]. Distributed generative modeling naturally aligns with this practice: specialized teams independently train domain-specific subsystem models without having to agree on a single architecture or training recipe. Likewise, teams can reuse third-party models whose data and training costs were borne elsewhere (*e.g.*, an open-source airfoil generator trained by a public research organization).

For these two reasons, we believe the distributed generative modeling approach is critically underappreciated.

2.3.1. Existing Distributed Modeling

An earlier approach to distributed generative modeling by Chen and Fuge [42] uses multiple submodels, coordinated

through a hierarchical relational graph. Crucially, this method requires all subsystem models to be trained jointly, meaning one cannot leverage the advantages of distributed modeling described in Section 2.3. Part-based approaches recently presented in computer graphics [43, 44] share this issue. Motivated by this limitation, we assume *pre-trained* generative submodels S_i and focus on how to coordinate them *without modification*. The resulting system-level designs must be system-level feasible, optimal, and diverse. To this end, we now examine three training regimes.

2.3.2. Data-Driven Training

Findings from recent work [38, 42] indicate that purely data-driven models can struggle with constraint satisfaction. A partial remedy is to inject labeled negative data, *i.e.*, designs that violate constraints. Regenwetter *et al.* show that this approach can improve the feasibility of synthesized designs [45].

2.3.3. Scoring-Augmented Data-Driven Training

Scoring-augmented approaches extend data-driven training with score-based loss terms targeting performance, diversity, or feasibility. Scores come from closed-form checks, surrogate models, or full simulators. For example, Chen and Ahmed extend on Determinantal Point Process (DPP)-based diversity scoring [46] to generate novel, high-performing designs [47, 48]. Regenwetter *et al.* show that such scoring-augmented generative models beat purely data-driven ones in validity and optimality and start to close the gap to optimizers like NSGA-II [49] and EPO [50].

2.3.4. Data-Free Training

More recently, fully data-free methods train generative models purely from scoring (without using any data), *e.g.* for topology optimization [51, 52].

Berzins *et al.* applied this to single-part shape generation, training a data-free shape-generative neural field using differentiable geometric objectives and constraints evaluated directly on a neural implicit surface [39]. To balance constraint, optimality, and diversity terms in a single loss, they use adaptive Augmented Lagrangian Method (ALM) [53], which replaces hand-tuned per-constraint penalties with three global hyperparameters ($\alpha, \gamma, \varepsilon$). The ALM schemes we used are summarized in Appendix D.

2.4. Differentiable Scoring

For scoring-augmented and data-free training, differentiable scores are especially attractive because they provide gradients for backpropagation in training. Diversity scores such as DPP [47] are differentiable when implemented carefully. For feasibility and performance, two main routes exist: (i) differentiable surrogate models, which require substantial training data but are broadly applicable, and (ii) native differentiable simulators. The latter have been extensively explored, *e.g.*, in aerodynamics (SU2 [54], DAFoam [55, 56]), solid mechanics (JAX-Finite Element Method (FEM) [57]), and rigid-body dynamics (JaxSim [58], MuJoCo MJX [59]).

Additionally, differentiable B-Rep-based Computer-Aided Design (CAD) tools have recently emerged [60, 61, 62, 63],

alongside growing interest in neural implicit Signed Distance Functions (SDFs) as flexible, robust, and differentiable CAD representations [64, 65, 66]. The methods proposed here are in principle agnostic to CAD representation type.

3. Methodology

First, we provide a brief overview of our multi-component UAV test case and its constituent pre-trained subsystem models. Then, we detail the baseline optimization algorithms (I.) and data-driven (II.) and data-free (III.) GLUE training paradigms.

3.1. UAV Design Problem

We use a fixed-wing UAV design problem as our case study. With coupled multi-physics, multiple subsystems, and high-dimensional design spaces, UAV design is representative of real engineering problems. The aerospace domain also offers extensive generative model literature [2, 29, 67, 68, 69], data, and benchmarks. Additionally, UAVs are small and affordable enough for eventual real-world validation.

We use a classical UAV decomposition into fuselage (outer skin), wings (lifting surfaces), and internal components. Internals are approximated by axis-aligned bounding boxes as placeholders for subsystems, with detailed component models (battery, electronics, *etc.*) left to future work. Here, all experiments instantiate the GLUE model on this parametrization, but GLUE could equally be applied to alternative decompositions (*e.g.*, blended-wing–body) and other problems (boats, buildings, *etc.*)

We formulate the UAV design task as a constrained optimization problem in a unified latent space $\mathcal{Z} \subset \mathbb{R}^{22}$ that collects all subsystem latents and coupling variables (see Figure 3). The full design space $\mathcal{X} \subset \mathbb{R}^{324}$ contains the full aircraft geometry parameters. Subsystem models $S_i : \mathcal{Z}_i \rightarrow \mathcal{X}_i$ and the differentiable geometry layer $\mathcal{G} : \mathcal{X} \rightarrow \mathbb{R}^{n_o+n_c}$ map latents to a single mass objective ($n_o = 1$) and constraints ($n_c = 5$). See Appendix E for a detailed account of \mathcal{Z} and \mathcal{X} and the formal problem statement. Performance issues related to aerodynamic stability and aircraft dynamics are omitted in this work.

The constraints are: (i) wing–fuselage interface fit (C_{bb}), (ii) consistent wing orientation (dihedral: C_{di}) and (iii) position (C_{wx}) on the fuselage, (iv) all internals contained inside the fuselage (C_{box-pl}), and (v) sufficient lift in level flight (C_{lift}). Note that all five constraints require explicit coordination between subsystems. Additionally, the objective (minimize O_{mass}) dictates that the fuselage must wrap tightly around the internals without violating C_{box-pl} . This implies that internals need to be arranged in a way that allows for a small fuselage. This coupling yields a highly nonconvex objective landscape with numerous local minima.

3.2. Subsystem Models

For the wing, we wrap the airfoil generator of Chen *et al.* [2] in a higher-level wing model. For the fuselage and internals, we train custom models to directly match our use case. Table 1 summarizes the three subsystem models. They differ substantially

Table 1: High-level comparison of subsystem models.

	Wing / Airfoil [2]	Fuselage	Internals
Model	MLP / CEBGAN	VAE	Autoreg. MLP
Dim(c_i)	1 / 3	-	N_{box}
Dim(z_i)	2 / -	4	4
Dim(x_i)	3 / 385	15	$6 \times N_{box}$
Losses	Lift Accuracy Diversity / OT [22, 70]	Recon. KL Div. LV [20]	Overlap Compactness Accurate Vol. Adjacent Div.
Data	Online / 995 (Opt.)	551 (Feas.)	Online
Cleanup	- / -	-	Grad. Desc.

to address the unique challenges of each subsystem. Complete descriptions are provided in Appendix B.

Here, these subsystem models are *pretrained* once and treated as *frozen* during coordination. Our method can interface with pretrained subsystem models *without* knowledge about their architectures, training data, or domain-specific tweaks. The only requirements we impose are (i) differentiability (support for automatic differentiation) and (ii) a smooth mapping $z_i \rightarrow x_i$ for subsystems subject to equality constraints (more on this later in Section 4.8.1).

3.3. Geometry Layer

All geometry-layer functionality is implemented in PyTorch [71], enabling native parallel execution and automatic differentiation. Details are given in Appendix L. The current implementation is tailored to this aircraft parametrization but could be generalized in future work. We now discuss three methods for latent space coordination in detail.

3.4. Method I: Optimization Algorithms

Optimization algorithms correspond to approach I in Figure 3, optimizing directly in the unified latent space \mathcal{Z} . We explicitly avoid optimization in the full design space \mathcal{X} (324-D), which would correspond to the monolithic setting we aim to avoid. We consider two optimizer classes.

3.4.1. Bayesian Optimization

Bayesian Optimization (BO) is robust to local minima and hence an attractive benchmark for both GLUE training regimes. However, vanilla BO is handicapped by poor scaling to high-dimensional problems, which may bias benchmarking toward GLUE. To address this issue, there are specialized BO variants [72, 73] that rely on pruning, embedding, or otherwise compressing the search space. Since we already operate in a compressed latent space, we expect little benefit from further dimensionality reduction. We therefore use Trust Region Bayesian Optimization (TuRBO) [74], which builds local trust regions with lightweight Gaussian Processes (GPs).

Additionally, convergence slows sharply as we add constraints, likely because the feasible hypervolume shrinks multiplicatively with each new constraint. For our highly coupled five-constraint aircraft problem, standard TuRBO is effectively unusable. To

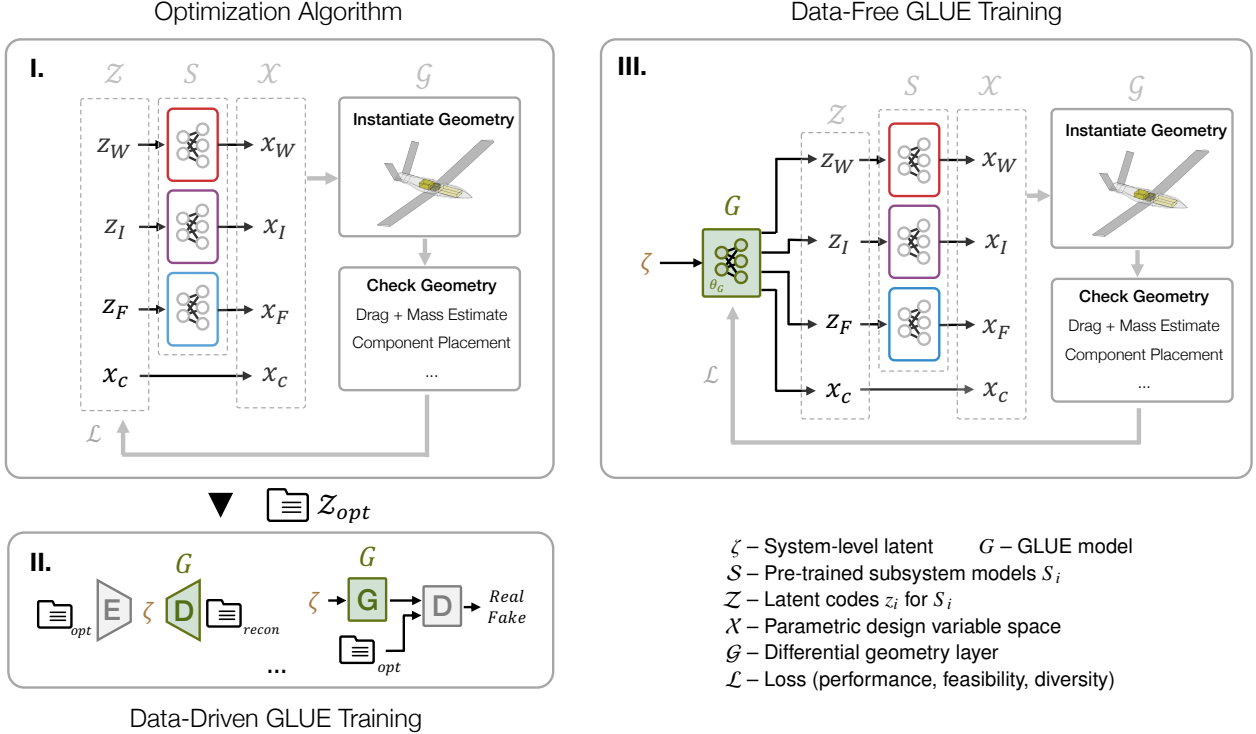


Figure 3: **I:** Optimization algorithm for creation of dataset of optimized designs (Z_{opt}) (e.g., gradient descent, Bayesian optimization, or evolutionary algorithms). **II:** Data-driven GLUE models (GAN, VAE, Denoising Diffusion Probabilistic Model (DDPM), ...) trained on large datasets obtained using I (optimization algorithms). **III:** Data-Free GLUE. Here, gradient descent on a loss $\mathcal{L} = \mathcal{L}_{feas} + \mathcal{L}_{perf} + \mathcal{L}_{div}$ is used to train GLUE model directly to map ζ to Z .

make BO more competitive in our later experiments, we address this by adding inner Gradient Descent (iGD) for equality constraints with known convex structure (C_{wx}, C_{di}, C_{lift}), yielding TuRBO-iGD. This accelerates convergence because TuRBO now only enforces two remaining constraints and operates in a reduced latent space (22 to 15 dimensions). More details can be found in Appendix J.

3.4.2. Gradient Descent

With this method, we perform gradient descent in the unified latent space Z using derivatives from the differentiable geometry layer. We minimize:

$$\mathcal{L} = O(z) + \sum_{k=1}^{n_c} \left(\lambda_k C_k(z) + \frac{\mu_k}{2} C_k(z)^2 \right) \quad (1)$$

with λ_k and μ_k updated based on constraint violations C_k (see Appendix D). Here, $O(z)$ is simply O_{mass} . Among all optimizers tested, ALM-Gradient Descent (GD) achieves the best combination of feasibility and mass, but remains sensitive to local minima, leading to a large set of diverse, locally optimal designs. Hyperparameters are hand-tuned to balance optimality, constraint satisfaction, and compute cost. Full settings and convergence criteria are given in Appendix J.

3.5. Method II: Data-Driven DD-GLUE

As introduced in the introduction, we propose a GLUE model G that maps a system-level latent ζ to subsystem latents z_i and

coupling variables x_C . Here, ζ is the unified latent code for the full aircraft. DD-GLUE corresponds to Approach II in Figure 3. To span common model architectures, we employ four data-driven GLUE models, the first two of which leverage negative data [45]:

cVAE A Conditional Variational Autoencoder (cVAE) with label conditioning.

MDD-GAN A Multi-Discriminator Generative Adversarial Network (MDD-GAN) with a 3-class discriminator (fake, feasible, infeasible).

OT-GAN An Optimal Transport Generative Adversarial Network (OT-GAN) using Sinkhorn divergences.

DDPM A DDPM with a cosine noise schedule [25].

For implementation details, see Appendix K. These models are designed to condition on velocity, altitude, internals mass, and internals volumes, but for the benchmarks shown here we train them at fixed (constant) conditions. For fair comparison, all data-driven models have similar or greater capacity than the 4.7M-parameter data-free GLUE model. For details, see Table K.14.

3.5.1. Training Data and Augmentation

We train DD-GLUE on designs optimized with ALM-GD, as it is the most compute-efficient of the tested optimizers and

yields high-quality samples. To improve constraint-satisfaction efficiency in benchmarking, augmentation is performed by sampling Gaussian jitter $\epsilon \sim \mathcal{N}(0, \sigma_{\text{aug}}^2)$ on the ALM-GD dataset. Each perturbed sample is then classified as feasible or infeasible (used in negative data models) via the geometry layer. σ_{aug} and N (yielding $N \times$ the original dataset size) are tuned for each model, with $N \leq 20$ to cap Graphics Processing Unit (GPU) memory use. As an alternative augmentation strategy, we consider storing pre-convergence samples along the ALM-GD trajectory. With this method, however, tiny steps near convergence produce many near-duplicates and thereby collapse diversity.

All data-driven GLUE models are hyperparameter-optimized so that quality differences to the data-free approach are not due to poor tuning (see Appendix K).

3.6. Method III: Data-Free GLUE

The core idea of DF-GLUE is to sample in ζ , propagate these samples through the frozen subsystem models S_i and geometry layer \mathcal{G} , and evaluate performance, constraint, and diversity scores. These scores are then backpropagated directly into the GLUE model (III in Figure 3).

Loss Formulation. Equation 2 shows the DF-GLUE training loss used in Algorithm 1

$$\begin{aligned} \mathcal{L}_{\text{total}} = & \lambda_{\text{perf}} (\lambda_m O_{\text{mass}} + \lambda_d O_d) \\ & + \lambda_{\text{bb}} C_{\text{bb}} + \lambda_{\text{wx}} C_{\text{wx}} + \lambda_{\text{di}} C_{\text{di}} + \lambda_{\text{lift}} C_{\text{lift}} + \lambda_{\text{box-pl}} C_{\text{box-pl}} \\ & + \lambda_{\text{DPP}, z_w} \text{DPP}(z_w) + \lambda_{\text{DPP}, z_F} \text{DPP}(z_F) + \lambda_{\text{DPP}, z_I} \text{DPP}(z_I) \\ & + \lambda_{\text{DPP}} \text{DPP}(\mathbf{x}) \\ & + \lambda_{\text{MI}} \mathcal{L}_{\text{MI}} \end{aligned} \quad (2)$$

where λ_{bb} , λ_{wx} , λ_{di} , λ_{lift} and $\lambda_{\text{box-pl}}$ are constraint multipliers updated via an ALM scheme (see Appendix D). We use a mass-only objective with $\lambda_m = 1$ and $\lambda_d = 0$ (no drag). The optional mutual information loss \mathcal{L}_{MI} encourages disentanglement in the system-level latent space and is enabled only in ablation runs (Section 4.8.1), not in benchmarking. Diversity is enforced via a DPP loss, either in design space \mathcal{X} with a single λ_{DPP} (benchmarking) or in latent space \mathcal{Z} with separate $\lambda_{\text{DPP}, z_w}$, $\lambda_{\text{DPP}, z_F}$, $\lambda_{\text{DPP}, z_I}$ (ablations) to control subsystem-wise diversity. The DPP weights and performance weight λ_{perf} are set manually and tune the trade-off between constraint satisfaction, performance, and diversity. All terms are currently scalarized into a single loss. Extending this to multi-objective formulations under varying conditions is left to future work [75, 38, 15, 76].

Architecture. For DF-GLUE, we use a Multi-Layer Perceptron (MLP)-based architecture with dedicated heads for each subsystem latents and placement. We use custom MLP initialization to prevent gradient vanishing with sigmoid and tanh activations. Details on the architecture and ablations are provided in Appendix C. This choice is not well suited to variable-length subsystem conditions and outputs (*e.g.*, varying volume-box sequences). Autoregressive, graph-based, or diffusion architectures may be better suited for multi-component generation but are left for future work.

Algorithm 1 DF-GLUE Training

DF-GLUE Training

Input: System-level latent ζ

Models: Coordinator model \mathcal{J} with parameters $\theta_{\mathcal{J}}$, subsystem models $\{S_i\}$, differentiable geometry layer \mathcal{G}

Parameters: Lagrange multipliers λ_k , performance weights λ_p

for epoch in epochs **do**

$(\{z_i\}, x_C) \leftarrow \mathcal{J}(\zeta)$ ▷ Coordinator forward pass

for each subsystem i **do**

$x_i \leftarrow S_i(z_i)$ ▷ Subsystem forward pass

end for

$\mathbf{x} \leftarrow \{x_i, x_C\}$ ▷ Instantiate designs

$O_p, C_k \leftarrow \mathcal{G}(\mathbf{x})$ ▷ Evaluate geometry

$\mathcal{L}_{\text{div}} \leftarrow \text{DPP}(\mathbf{z})$ ▷ Compute DPP scores

$\mathcal{L}_{\text{feas}} \leftarrow \sum_k \lambda_k C_k$ ▷ Compute feasibility loss

$\mathcal{L}_{\text{perf}} \leftarrow \sum_p \lambda_p O_p$ ▷ Compute performance loss

 Backpropagate $\mathcal{L}_{\text{feas}} + \mathcal{L}_{\text{perf}} + \mathcal{L}_{\text{div}}$ and update $\theta_{\mathcal{J}}$

$\lambda_k \leftarrow \text{ALM}(\lambda_k, C_k)$ ▷ Update multipliers

end for

Experimental Details. We use a system-level latent dimension of $\text{dim}(\zeta) = 2$ for visualization experiments and $\text{dim}(\zeta) = 4$ otherwise. We train with a batch size of 1296 for 2500 epochs. Unless mentioned otherwise, operating conditions are fixed to case 1 (see Appendix G). In principle, GLUE can be trained over broad condition ranges for true inverse design, which we leave for future work.

4. Results

4.1. Evaluation Metrics

Feasibility. A sample is feasible if inequality constraints ($C_{\text{box-pl}}$ and C_{bb}) satisfy ≤ 0 , and equality constraints satisfy their constraint-specific tolerances. These are $C_{\text{wx}} \leq 0.02 \cdot b$ (2% of wing span), $C_{\text{di}} \leq \{0.5^\circ, 2^\circ\}$ (front/rear), and $C_{\text{lift}} \leq 0.02 \cdot L_{\text{req}}$ (2% of lift requirement). Feasibility is assessed with an additional numerical tolerance of 10^{-3} .

Single-Objective Optimality. In this study, we minimize O_{mass} only. The objective is made dimensionless by normalizing with internal mass, *i.e.*, the reported figures do not directly correspond to absolute aircraft mass.

Diversity. We measure design variety via a DPP score in $[0, \infty)$, where 0 indicates high diversity and ∞ identical samples. For implementation details, see Appendix F.

Compute Efficiency. We report two complementary cost views. *Geometry evaluations* count forward passes through the subsystem models S_i and the geometry layer \mathcal{G} . *Floating Point Operations (FLOPs)* measure total compute and include backpropagation, whose share differs by method. For DD-GLUE variants (II.), compute includes training and dataset creation using ALM-GD. Separately, we report the *wall-clock time* required to optimize (I.) and train (II. and III.).

We assess GLUE by uniformly sampling ζ (1000 samples per GLUE model training seed) and instantiating designs via a batched forward pass through the GLUE model and subsystem models. We then score each design in the geometry layer for objective value, feasibility, and compute diversity.

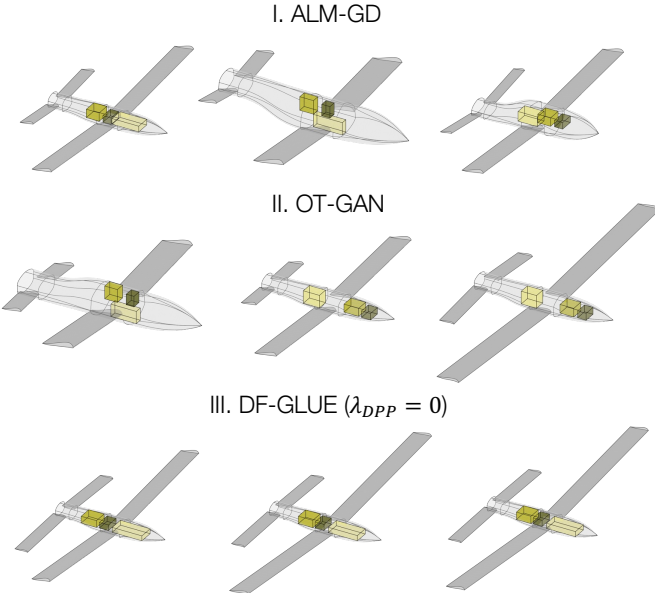


Figure 4: Exemplar aircraft designs for methods I, II and III.

4.2. Visual Comparison

We start with a qualitative look at selected samples in Figure 4. ALM-GD (I.) often converges to suboptimal designs. For example, stacked internals instead of a single row (the middle sample in Figure I.20) prevent further fuselage shrinkage and yield suboptimal O_{mass} . Locally, there is no gradient signal to move the boxes into a single row, so ALM-GD gets trapped in a local minimum. DD-GLUE variants (II., here only OT-GAN) are trained on ALM-GD data and therefore tend to reproduce similar designs. In contrast, DF-GLUE (III.) virtually collapses to the global optimum when trained without diversity losses, as shown here. A more detailed visual comparison can be found in Appendix I.

4.3. Basin Connectivity

In our experiments, GLUE demonstrates the capacity to *bridge distinct design basins* by briefly passing through infeasible or suboptimal regions. This holds when multiple basins exist in the underlying data or diversity is explicitly incentivized (e.g., via $\lambda_{\text{DPP},\zeta}$). In our UAV case, transitions either remain feasible but highly suboptimal, or stay near-optimal with a short, strongly infeasible leap. In practice, training yields an intermediate path, governed by hyperparameters that balance objective and constraint penalties. Figure 5 illustrates this behavior. During internals reordering, the model slightly inflates the fuselage to lower penalty while still tolerating a small $C_{\text{box-pl}}$ violation.

4.4. Benchmarking

Experiment Details. GLUE is assessed using 10 seeds and 1000 uniform ζ samples per seed. We report $P5/P95$ percentiles across the resulting 10k designs. Feasibility is reported for the mean, best, and worst seed out of 10. Figure 6 reports a single condition set (case 1, see Appendix G) For a high-level cross-case comparison, see Appendix H. Since TuRBO-iGD retains only its best designs, we score it on its top 1% performers for fairness. DD-GLUE variants use the full training set to maximize constraint satisfaction. MDD-GAN is the only exception, as it reaches best feasibility at 80% (see Figure 7). We suspect this may result from the interplay between augmentation hyperparameters (σ_{aug} and N , see Appendix K) and dataset structure, which together determine the positive-to-negative data ratio.

Findings. As seen in Figure 6, TuRBO-iGD underperforms in optimality on this high-dimensional, tightly constrained setting due to the fundamental shortcomings of BO. ALM-GD can find strong designs but is sensitive to local minima, as indicated by the high objective variance across ~ 70 k runs and low DPP score, which implies high diversity. On the other hand, DF-GLUE with $\lambda_{\text{DPP}} = 0$ *robustly collapses to the global optimum* and achieves near-perfect feasibility. Sweeping λ_{DPP} and λ_{perf} (see table in Figure 6) traces a Pareto front indicating the trade-off between diversity on one hand and optimality and feasibility on the other. At equal diversity, DF-GLUE is near-optimizer-feasible and exceeds all data-driven feasibility. The DD-GLUE variants roughly replicate optimality and diversity of the underlying ALM-GD data, which is to be expected. Among the

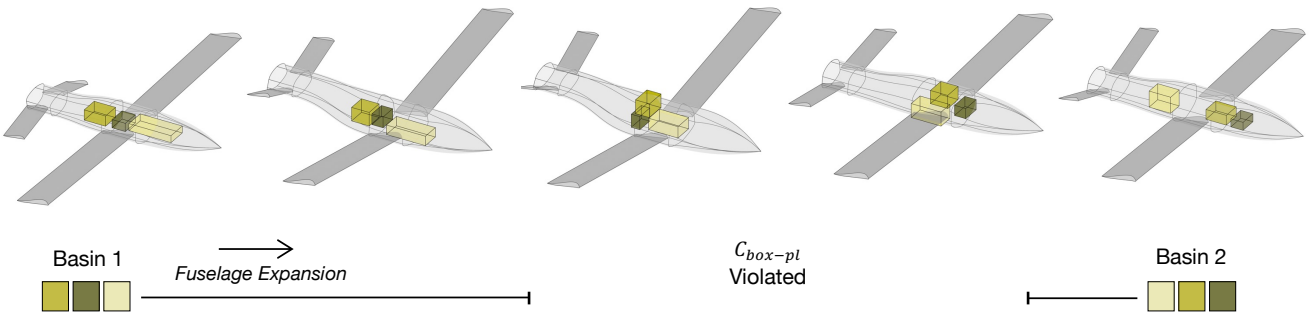


Figure 5: Traversing non-feasible, non-optimal design region to achieve diversity.

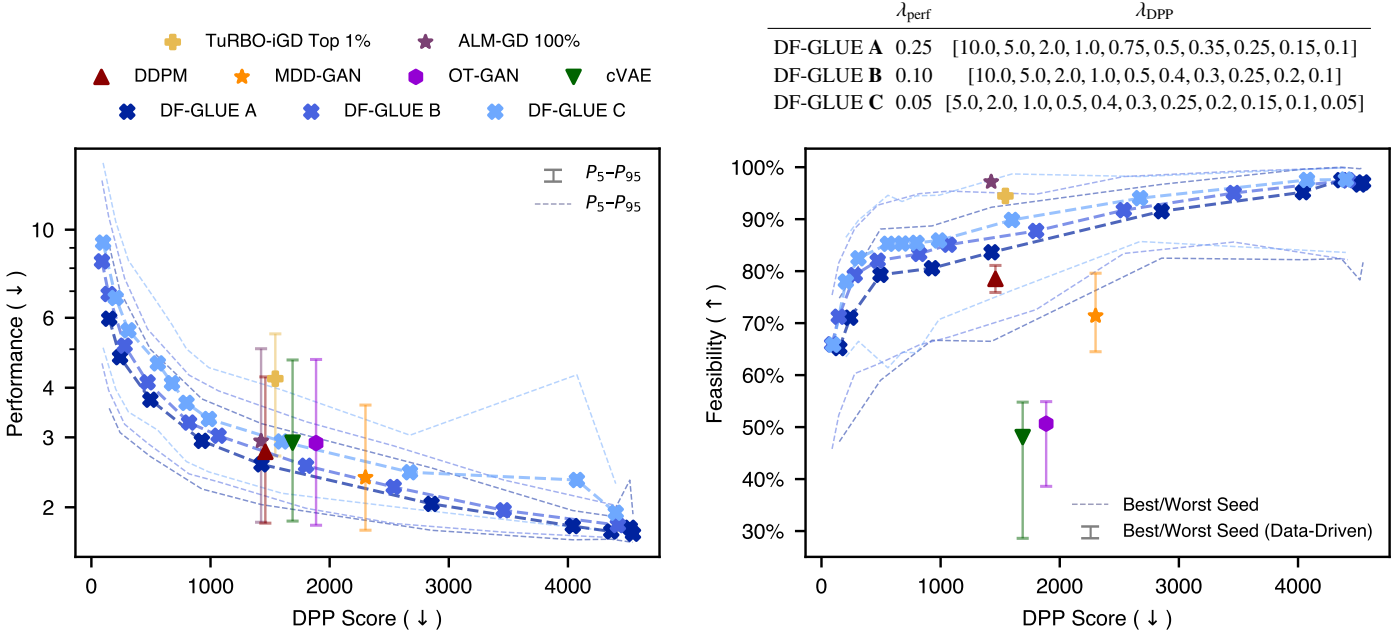


Figure 6: Trade-offs between optimality, feasibility, and diversity for ALM-GD, TuRBO-iGD, data-driven GLUE models (cVAE, OT-GAN, MDD-GAN, DDPM) and data-free GLUE model (DF-GLUE). DF-GLUE is swept across multiple hyperparameter combinations to showcase the full range of accessible trade-offs between diversity, optimality, and feasibility. For generative models, each marker summarizes 10 seeds \times 1000 samples/seed. Vertical bars show 5th to 95th percentile in performance across designs. Feasibility bars show best/worst feasibility out of 10 seeds.

data-driven models, DDPM is strongest in feasibility, achieving similar feasibility to DF-GLUE. However, the DDPM achieves this at significantly higher computational cost than DF-GLUE, as detailed in the next section.

4.5. Computational Efficiency

Experiment Details. We use the same sampling protocol and summary statistics as in Section 4.4 (10 seeds, 1000 ζ samples/seed, $P5/P95$ for performance and mean/best/worst-seed feasibility, conditions from case 1). Figure 7 shows optimality and feasibility with varying training budget. DF-GLUE is trained for 600–2500 epochs ($\lambda_{DPP} = 0$). The DD-GLUE variants are trained on ALM-GD subsets from 5% to 100% of the ~ 70 k-design dataset. The shown ALM-GD datapoint corresponds to the full dataset. (Note: If only a single design is needed, ALM-GD remains the most compute-efficient per design (≈ 1 TFLOP and < 3 k geometry evaluations per run).

Findings. We find that in this UAV study, optimality is rather easy to learn for the data-driven models. Even when trained

on 5% of data (~ 3.5 k designs), the distribution of optimality closely matches the underlying dataset. In contrast, learning our coupled, non-convex constraints is highly data-intensive. For all data-driven models, feasibility scales extremely weakly with increasing compute budgets. In contrast, the gradient-driven DF-GLUE reaches high feasibility using orders of magnitude less compute (see Figure 7).

4.6. Wall-Clock Time

Table 2 reports wall-clock times for optimization (I.) and training (II. and III.). ALM-GD and DF-GLUE are run with profiling for the analysis in Figure 7, which slightly increases their runtimes. ALM-GD and Bayesian optimization show large seed-to-seed runtime variance. Drivers are large trajectory differences based on initial seed, auto-stopping (ALM-GD), and varying GPs fitting complexity (BO).

Most strikingly, DF-GLUE is so training-efficient that it produces a full generative model in less time than the optimization algorithms need to generate a single feasible sample.

Table 2: Wall-clock times and hardware configurations. Prof. = profiling, Auto = autostopping.

Method	Hardware	Avg \pm SD	Min	Max	Prof.	Auto
TuRBO-iGD	2 CPU, 2GB	7h22m \pm 52m	5h35m	10h38m	<input checked="" type="checkbox"/>	<input checked="" type="checkbox"/>
ALM-GD	1 CPU, 4GB	54m \pm 18m	10m12s	2h36m	<input checked="" type="checkbox"/>	<input checked="" type="checkbox"/>
DDPM	RTX 4090	48m \pm 2m	45m57s	52m36s	<input checked="" type="checkbox"/>	<input checked="" type="checkbox"/>
MDD-GAN	RTX 4090	25m54s \pm 5s	25m47s	26m00s	<input checked="" type="checkbox"/>	<input checked="" type="checkbox"/>
OT-GAN	RTX 4090	23m41s \pm 2s	23m38s	23m43s	<input checked="" type="checkbox"/>	<input checked="" type="checkbox"/>
cVAE	RTX 4090	13m03s \pm 6s	12m55s	13m10s	<input checked="" type="checkbox"/>	<input checked="" type="checkbox"/>
DF-GLUE	RTX 4090	10m31s \pm 5s	10m21s	10m36s	<input checked="" type="checkbox"/>	<input checked="" type="checkbox"/>

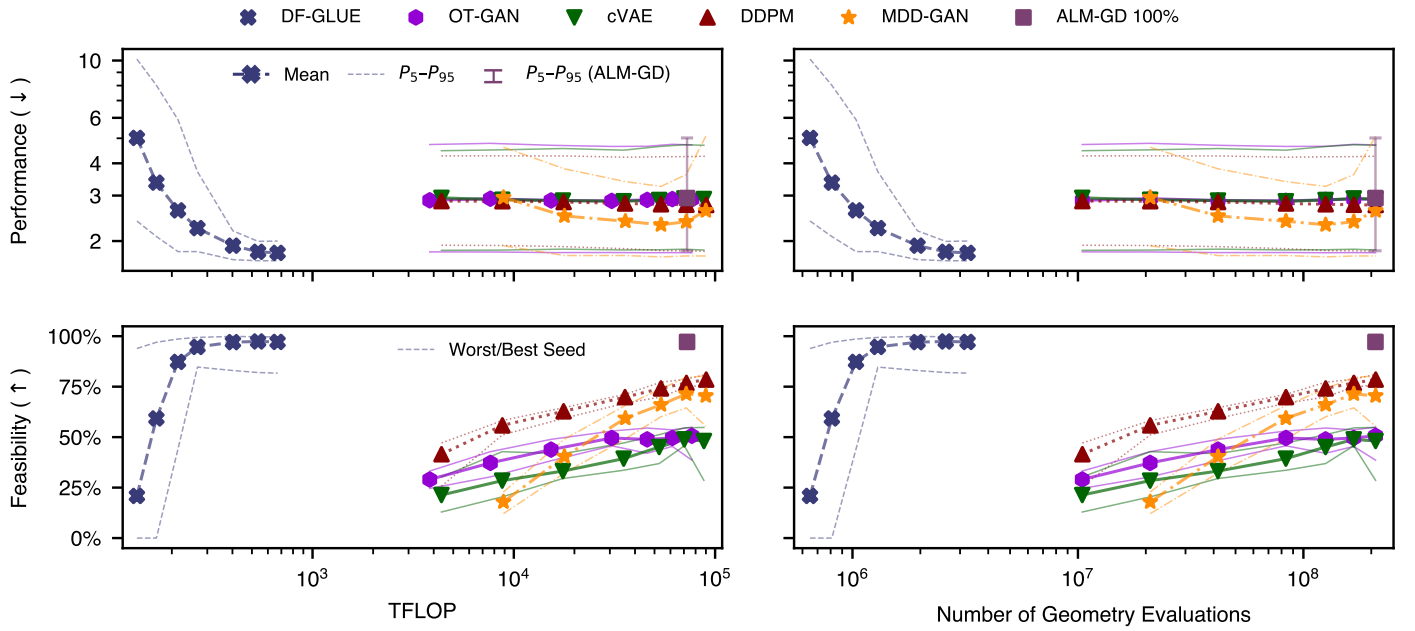


Figure 7: Comparison of optimality, feasibility, and mean constraint violation against computational cost. DF-GLUE ($\lambda_{\text{DPP}} = 0$) attains high feasibility and global optimality at orders of magnitude lower cost than DD-GLUE training. For DF-GLUE, each marker summarizes 10 seeds for different amounts of training epochs. For data-driven models, each marker summarizes 10 seeds at given data subset (5 % – 100 %) for training.

4.7. Discussion

Bayesian Optimization Limitations. TuRBO fails to produce high-quality designs even with additional modifications (iGD) to deal with equality constraints. We attribute this to BOs fundamental limitations for high-dimensional problems. This observation confirms our view that the UAV design problem is a non-trivial benchmark.

Data-Driven Models. On our UAV design problem, DD-GLUE variants learn optimal, diverse solutions from relatively few samples, but they exhibit poor ability to recover hard-to-learn constraints (Section 4.4) even with extensive datasets (Section 4.5). This is consistent with prior observations that learning feasibility purely from data is non-trivial (see Section 2.3.2).

4.7.1. DD-GLUE

Optimization Robustness. Given $\lambda_{\text{DPP}} = 0$, we observe DF-GLUE robustly collapses to the globally optimal constrained solution across seeds, matching the best designs found by traditional optimizers (see Sections 4.2, 4.4, 4.5). We attribute this to reduced sensitivity to local minima in over-parametrized network parameter space (4.7M parameters) versus latent-space optimization in \mathcal{Z} (22-D).

Tractable Constraint Learning. DF-GLUE learns feasibility far more efficiently than DD-GLUE variants, requiring orders of magnitude fewer geometry evaluations and FLOPs (Sec. 4.5). It trains faster than ALM-GD can return one feasible design (Sec. 4.6). (Note: ALM-GD runs on CPU, while DF-GLUE is trained on GPU. But, in practice, our ALM-GD shows no wall-clock gain from parallelization.)

We attribute this to *information efficiency*. Data-driven training keeps only final converged ALM-GD designs, discarding

optimizer trajectories. Additionally, it lacks access to local gradients. DF-GLUE instead backpropagates through differentiable objectives, maximizing learning signal and fully utilizing each forward pass.

Additionally, we see headroom for further speedups. We find that training convergence speed is insensitive to increases in batch size. This implies that DF-GLUE training is not bottlenecked by information acquisition through forward passes, but rather training dynamics (ALM weight growth and primal learning-rate schedule). We hypothesize that studying these dynamics could compress the current DF-GLUE training times markedly at equal solution quality.

Explicit Diversity Control. A further advantage of DF-GLUE is explicit, user-specified control of the trade-off between diversity and robust collapse to the global optimum (with $\lambda_{\text{DPP}} = 0$). Data-driven models lack this explicit control. A similar result could be achieved with dataset filtering, but this would further degrade compute efficiency.

4.8. Data-Free GLUE: Ablation Studies

We now shift focus to examine two notable points in DF-GLUE training. For both experiments, please refer to Appendix A for hyperparameters and Appendix F for more on DPP scoring.

4.8.1. Effect of Subsystem Model Smoothness

Experiment. We compare two fuselage models trained on the same dataset, differing only in whether Spectral Normalization (SN) is enabled during training. Enabling SN constrains the Lipschitz constant of the fuselage sub-model. For experiment details, please refer to Appendix A and Appendix F. Table 3 shows

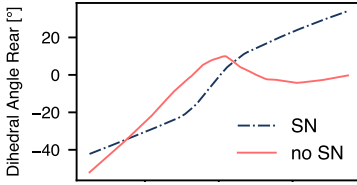


Figure 8: Mapping $z_{F,0} \xrightarrow{S_F} x_{F,9}$ is smoothed and meaningful with SN.

Table 3: Effect of Spectral Normalization of fuselage subsystem model S_F . Lack of subsystem model smoothness undermines DF-GLUE’s ability to satisfy coupled equality constraints. IA = Inner Adam, SN = Spectral Normalization.

SN	IA	$O_{\text{mass}} (\downarrow)$	$C_{\text{wx}} (\uparrow)$	$C_{\text{di}} (\uparrow)$	$C_{\text{lift}} (\uparrow)$	$C_{\text{bb}} (\uparrow)$	$C_{\text{box-pl}} (\uparrow)$	DPP (\downarrow)
✗	No	8.52	0.5%	0.2%	23.1%	83.7%	78.1%	3668
✗	Yes	11.9	0.0%	0.1%	3.4%	96.9%	93.2%	3677
✓	No	2.36	98.4 %	66.8%	94.7%	100 %	96.8 %	3840
✓	Yes	2.36	98.1%	73.8%	95.1%	100 %	94.9%	3798

that without SN on S_F , learning the equality constraints (C_{wx} , C_{di} , C_{lift}) is virtually intractable. The resulting optimization largely collapses into enforcing C_{wx} and C_{di} , and O_{mass} degrades markedly, indicating substantial benefits to spectrally normalizing subsystem models. Unfortunately, SN can also reduce subsystem output diversity depending on the model architecture, as seen in Figure 9.

Discussion. SN makes the coordination problem easier by (i) smoothing the mapping $z_F \rightarrow x_F$, (ii) allowing the minimum-volume loss [20] used to train S_F to function and thereby promoting disentanglement, and (iii) reducing output diversity by limiting sharp fitting to the training distribution. Effects (i) and (ii) can be observed in Figure 8. Together, these three effects make learning of hard-to-satisfy equality constraints tractable. This highlights that subsystem model quality is a primary driver of ease of coordination. Ideally, subsystems should combine diversity with a smooth, disentangled mapping $z_i \rightarrow x_i$.

Note that this does not apply to the GLUE model itself, where SN would hinder rapid traversal through infeasible regions needed for basin bridging (Figure 5).

4.8.2. Mode Collapse from Equality Constraints

Next, we find that equality constraints can induce mode collapse during DF-GLUE training. Without any countermeasures, equality constraints are associated with an infinitesimally small feasible hypervolume in \mathcal{Z} . Figure 10 illustrates this for the dihedral equality constraint C_{di} by plotting angle violation against the scaled constraint loss. With a stiff weight $\lambda_{\text{di}} \gg 1$, any arbitrarily small angle violation incurs a large penalty. Once a feasible point is reached, leaving it becomes prohibitively expensive, trapping optimization in a local minimum and preventing progress on optimality, diversity, and other constraints. We compare three approaches to mitigate this issue:

Inner Adam. Using a dedicated optimizer (Adam), we back-propagate selected equality constraints only through the GLUE output layers controlling their relevant variables. For example, routing C_{wx} and C_{di} only through wing placement output layers prevents DF-GLUE from correcting misplaced wings by adapting fuselages (see Fig. C.15). While effective, this requires prior knowledge of variable-constraint dependencies.

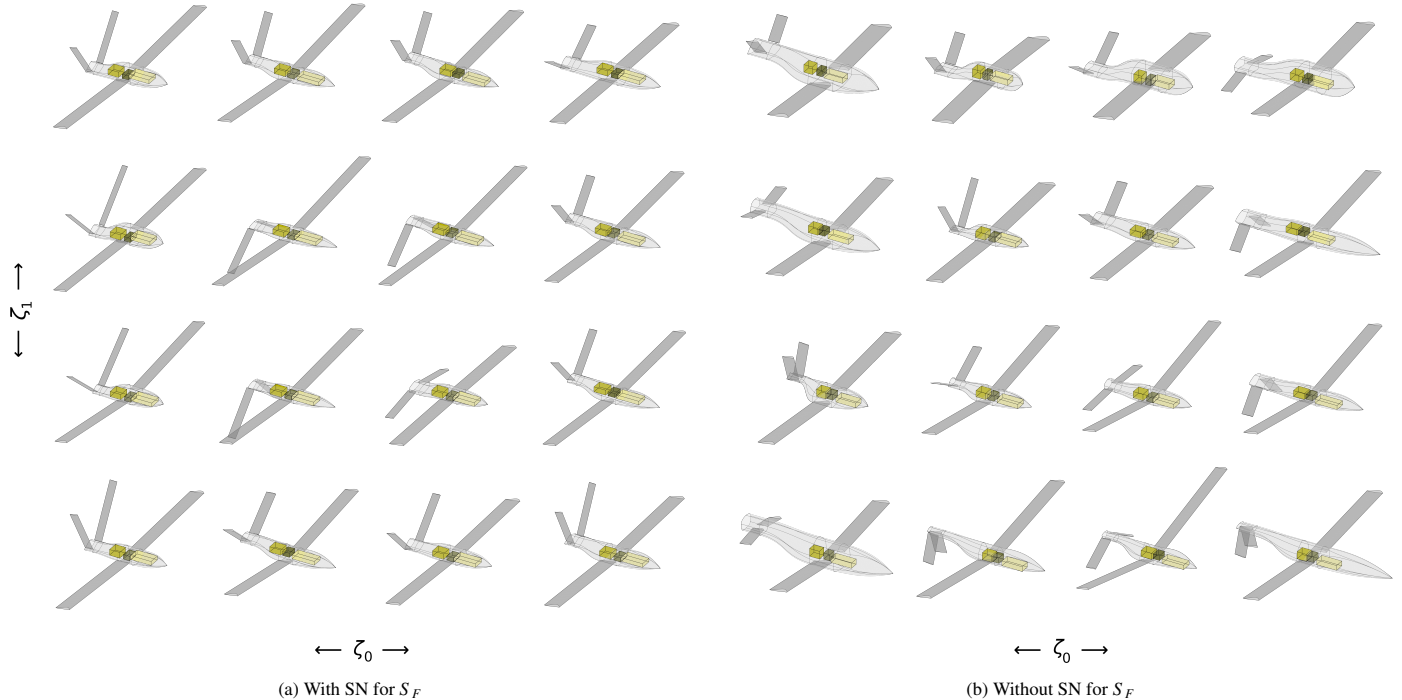


Figure 9: Sweep of system-level latent space ζ comparing fuselage model SN effects. (a) With SN enabled, the smooth subsystem model allows more precise constraint satisfaction and optimality. (b) Without SN, we observe increased diversity in fuselage model outputs.

Equality Constraint Tolerancing. We soften equalities into tolerance bands so the optimizer can make incremental progress without immediate large penalty spikes (see Figure 10). We use C_{wx} within 2% of span and $C_{di} \leq \{0.5^\circ/2^\circ\}$ (front/rear dihedral).

Smoothing of Equality Constraints. We replace the ReLU baseline with an L1-Huber activation function for equality constraints (ϕ_{eq}). This allows the optimizer to pursue optimality, diversity, and other constraints without incurring a large loss spike at the constraint boundary (see Figure 10).

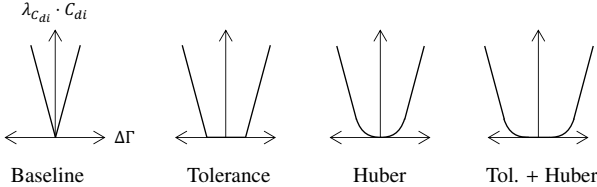


Figure 10: Tolerance and smoothing of equality constraints

Table 4: Mode collapse ablation study for case 1b. Each variant with 10 seeds and 1000 samples per seed. GLUE model with $\dim(\zeta) = 2$. DPP measured on z_F . High DPP scores and O_{mass} are indicative of mode collapse. Baseline (first row) shows severe mode collapse. IA = Inner Adam. Tol. = Tolerance, ϕ_{eq} = Equality constraint loss smoothing function.

IA	Tol.	ϕ_{eq}	Feas. (\uparrow)	DPP (\downarrow)	$O_{\text{mass}} (\downarrow)$
\times	<u>Zero</u>	<u>ReLU</u>	11.6 %	50106	23.82
\checkmark	Normal	Huber	69.9 %	7	4.15
\checkmark	<u>Zero</u>	Huber	75.5 %	54	4.20
\checkmark	<u>Zero</u>	<u>ReLU</u>	73.7 %	112	4.30
\times	Normal	Huber	59.6 %	9557	4.47
\times	Normal	<u>ReLU</u>	55.8 %	19641	5.03

Discussion. Table 4 shows that the baseline (no inner Adam, zero tolerance, ReLU) collapses into a poor local minimum (high DPP, low feasibility, high mass). Adding tolerancing and Huber smoothing improves feasibility and objective despite still-elevated DPP scores. Inner Adam yields the largest gain, and combining it with tolerancing and smoothing is best. When an inner solver is infeasible, tolerancing and smoothing remain broadly applicable mitigations for equality constraints.

5. Conclusion

We propose GLUE models. These orchestrate *frozen, pre-trained* subsystem models (wings, fuselage, internals) to generate feasible, high-performing, and diverse system-level designs. We showcase this method on a high-dimensional, non-convex, tightly constrained UAV problem that approximates real engineering settings. Two training paradigms are compared: (*i*) Data-Driven, which uses state-of-the-art generative architectures (cVAE, MDD-GAN, OT-GAN, DDPM) as GLUE models and is trained on datasets of optimized designs, and (*ii*) Data-Free, which uses a differentiable geometry layer to backpropagate constraint and objective gradients directly into the GLUE model, eliminating the need for pre-generated datasets. Both paradigms

are benchmarked against baseline latent-space optimization algorithms (TuRBO-iGD and ALM-GD).

When trained without an explicit diversity loss, DF-GLUE more reliably converges to the global optimum than both optimizers, with ALM-GD particularly prone to getting trapped in local minima. However, while DF-GLUE shows strong performance and promising feasibility, optimization algorithms still achieve slightly stricter satisfaction of constraints. DF-GLUE is orders of magnitude more computationally efficient than data-driven GLUE models. It reuses gradient information at every geometry evaluation, whereas the optimizers used to generate training data for data-driven methods discard intermediate trajectories and retain only final designs. Ablation studies show that subsystem model quality strongly influences DF-GLUE’s ability to produce feasible designs. Enforcing smoother $z_i \rightarrow x_i$ mappings (*e.g.*, via SN in the fuselage model) improves constraint satisfaction and optimality at a slight cost of subsystem diversity. Mode collapse induced by equality constraints is best mitigated by inner gradient-descent solvers on selected constraint subsets, with additional gains from constraint smoothing and tolerancing.

This work outlines a path toward modular, collaborative workflows in which specialized teams develop subsystem models that are later integrated without retraining. Our approach is especially attractive when subsystem development costs can be amortized across multiple projects or when reusing proprietary or open-source third-party models.

Some limitations remain. First, data-free training presumes differentiable simulators and constraint checkers, which may not be available in every domain. Differentiable surrogates can address this gap but reintroduce data-generation cost. Second, the suitability of our method with diffusion models for subsystems has yet to be explored. Third, the work presented here is limited to single-objective optimization. For multi-objective optimization, specialized methods [75] are preferable to conflating competing objectives into a single weighted loss. Finally, results are limited to a single predefined UAV parametrization. Achieving true diversity across UAV concepts and extending our method to other engineering problems requires a generalizable geometry layer.

Code and Data Availability

Our code will be made publicly accessible shortly under:
github.com/IDEALLab/glue

References

- [1] W. Para, P. Guerrero, T. Kelly, L. Guibas, P. Wonka, Generative layout modeling using constraint graphs, in: 2021 IEEE/CVF International Conference on Computer Vision (ICCV), IEEE, Montreal, QC, Canada, 2021, pp. 6670–6680. doi:10.1109/ICCV48922.2021.00662. 1, 2
- [2] W. Chen, K. Chiu, M. D. Fuge, Airfoil design parameterization and optimization using b  ezier generative adversarial networks, *AIAA Journal* 58 (11) (2020) 4723–4735. doi:10.2514/1.J059317. 1, 2, 3, 4, 15, 16
- [3] B. Sanchez-Lengeling, A. Aspuru-Guzik, Inverse molecular design using machine learning: Generative models for matter engineering, *Science* 361 (6400) (2018) 360–365. doi:10.1126/science.aat2663. 1, 2
- [4] V. Balmer, S. V. Kuhn, R. Bischof, L. Salamanca, W. Kauffmann, F. Perez-Cruz, M. A. Kraus, Design space exploration and explanation via conditional variational autoencoders in meta-model-based conceptual design of pedestrian bridges, *Automation in Construction* 163 (2024) 105411. doi:https://doi.org/10.1016/j.autcon.2024.105411. 1
- [5] T. Brzin, M. Brojan, Using a generative adversarial network for the inverse design of soft morphing composite beams, *Engineering Applications of Artificial Intelligence* 133 (2024). doi:10.1016/j.engappai.2024.108527. 2
- [6] Y. Tang, K. Kojima, T. Koike-Akino, Y. Wang, P. Wu, Y. Xie, M. H. Tahersima, D. K. Jha, K. Parsons, M. Qi, Generative deep learning model for inverse design of integrated nanophotonic devices, *Laser & Photonics Reviews* 14 (12) (2020). doi:10.1002/lpor.202000287. 2
- [7] A. Kadan, K. Ryczko, E. Lloyd, A. Roitberg, T. Yamazaki, Guided multi-objective generative ai to enhance structure-based drug design, *Chemical Science* 16 (29) (2025) 13196–13210. doi:10.1039/D5SC01778E. 2
- [8] K. Zuo, S. Bu, W. Zhang, J. Hu, Z. Ye, X. Yuan, Fast sparse flow field prediction around airfoils via multi-head perceptron based deep learning architecture, *Aerospace Science and Technology* 130 (2022). doi:10.1016/j.ast.2022.107942. 2
- [9] H. Karali, M. U. Demirezen, M. A. Yukselen, G. Inalhan, Design of a deep learning based nonlinear aerodynamic surrogate model for uavs, in: AIAA Scitech 2020 Forum, American Institute of Aeronautics and Astronautics, 2020. doi:10.2514/6.2020-1288. 2
- [10] J. Tao, G. Sun, Application of deep learning based multi-fidelity surrogate model to robust aerodynamic design optimization, *Aerospace Science and Technology* 92 (2019) 722–737. doi:10.1016/j.ast.2019.07.002. 2
- [11] L. Regenwetter, C. Weaver, F. Ahmed, Framed: An automl approach for structural performance prediction of bicycle frames, *Computer-Aided Design* 156 (2023) 103446. doi:https://doi.org/10.1016/j.cad.2022.103446. 2
- [12] T. Benamara, P. Breitkopf, I. Lepot, C. Sainvitu, P. Villon, Multi-fidelity pod surrogate-assisted optimization: Concept and aero-design study, *Structural and Multidisciplinary Optimization* 56 (6) (2017) 1387–1412. doi:10.1007/s00158-017-1730-4. 2
- [13] S. G. Kontogiannis, M. A. Savill, A generalized methodology for multidisciplinary design optimization using surrogate modelling and multifidelity analysis, *Optimization and Engineering* 21 (3) (2020) 723–759. doi:10.1007/s11081-020-09504-z. 2
- [14] W. Yao, X. Chen, Q. Ouyang, M. Van Tooren, A surrogate based multistage-multilevel optimization procedure for multidisciplinary design optimization, *Structural and Multidisciplinary Optimization* 45 (4) (2012) 559–574. doi:10.1007/s00158-011-0714-z. 2
- [15] S. Massoudi, C. Picard, J. Schiffmann, An Integrated Approach to Designing Robust Gas-Bearing Supported Turbocompressors Through Surrogate Modeling and Constrained All-At-Once Multi-Objective Optimization, *Journal of Mechanical Design* 146 (121706) (2024). doi:10.1115/1.4065823. 2, 6
- [16] I. Goodfellow, J. Pouget-Abadie, M. Mirza, B. Xu, D. Warde-Farley, S. Ozair, A. Courville, Y. Bengio, Generative adversarial networks, *Communications of the ACM* 63 (11) (2020) 139–144. doi:10.1145/3422622. 2
- [17] D. P. Kingma, M. Welling, Auto-encoding variational bayes, in: International Conference on Learning Representations, 2014. doi:10.48550/arXiv.1312.6114. 2
- [18] A. Cobb, A. Roy, D. Elenius, K. Koneripalli, S. Jha, On diverse system-level design using manifold learning and partial simulated annealing, *Proceedings of the Design Society* 2 (2022) 1541–1548. doi:10.1017/pds.2022.156. 2, 3
- [19] L. Regenwetter, A. H. Nobari, F. Ahmed, Deep generative models in engineering design: A review, *Journal of Mechanical Design* 144 (7) (2022). doi:10.48550/arXiv.2110.10863. 2
- [20] Q. Chen, M. Fuge, Compressing latent space via least volume, in: The Twelfth International Conference on Learning Representations, 2024. doi:10.48550/arXiv.2404.17773. 2, 4, 10, 16
- [21] X. Chen, Y. Duan, R. Houthooft, J. Schulman, I. Sutskever, P. Abbeel, Infogan: Interpretable representation learning by information maximizing generative adversarial nets, in: Advances in Neural Information Processing Systems, Vol. 29, 2016. doi:10.48550/arXiv.1606.03657. 2

[22] A. Genevay, G. Peyré, M. Cuturi, Learning generative models with sinkhorn divergences, in: International Conference on Artificial Intelligence and Statistics, PMLR, 2018, pp. 1608–1617. doi:10.48550/arXiv.1706.00292. 2, 4, 32

[23] M. Arjovsky, S. Chintala, L. Bottou, Wasserstein generative adversarial networks, in: International Conference on Machine Learning, PMLR, 2017, pp. 214–223. doi:10.48550/arXiv.1701.07875. 2

[24] Q. Chen, P. Tsilifis, M. Fuge, Bayesian inverse problems with conditional sinkhorn generative adversarial networks in least volume latent spaces, *Neural Networks* 191 (Nov. 2025). doi:10.1016/j.neunet.2025.107740. 2

[25] J. Ho, A. Jain, P. Abbeel, Denoising diffusion probabilistic models, *Advances in Neural Information Processing Systems* 33 (2020) 6840–6851. doi:10.48550/arXiv.2006.11239. 2, 5, 32

[26] J. Song, C. Meng, S. Ermon, Denoising diffusion implicit models, in: International Conference on Learning Representations, 2021. doi:10.48550/arXiv.2010.02502. 2

[27] F. Mazé, F. Ahmed, Diffusion models beat gans on topology optimization, *Proceedings of the AAAI Conference on Artificial Intelligence* 37 (8) (2023) 9108–9116. doi:10.1609/aaai.v37i8.26093. 2, 3

[28] J.-H. Bastek, W. Sun, D. Kochmann, Physics-informed diffusion models, in: The Thirteenth International Conference on Learning Representations, 2025. doi:10.48550/arXiv.2403.14404. 2

[29] C. Diniz, M. Fuge, Optimizing diffusion to diffuse optimal designs, in: AIAA SCITECH 2024 Forum, American Institute of Aeronautics and Astronautics, 2024. doi:10.2514/6.2024-2013. 2, 3, 4

[30] G. Giannone, A. Srivastava, O. Winther, F. Ahmed, Aligning optimization trajectories with diffusion models for constrained design generation, in: Thirty-seventh Conference on Neural Information Processing Systems, 2023. doi:10.48550/arXiv.2305.18470. 2

[31] E. Herron, J. Rade, A. Jignasu, B. Ganapathysubramanian, A. Balu, S. Sarkar, A. Krishnamurthy, Latent diffusion models for structural component design, *Computer-Aided Design* 171 (2024). doi:10.1016/j.cad.2024.103707. 2

[32] E. J. Cramer, J. E. Dennis, Jr., P. D. Frank, R. M. Lewis, G. R. Shubin, Problem formulation for multidisciplinary optimization, *SIAM Journal on Optimization* 4 (4) (1994) 754–776. doi:10.1137/0804044. 2

[33] J. Sobieszczański-Sobieski, Multidisciplinary design optimization: An emerging new engineering discipline, in: J. Herskovits (Ed.), *Advances in Structural Optimization*, Vol. 25, Springer Netherlands, pp. 483–496. doi:10.1007/978-94-011-0453-1_14. 2

[34] J. R. R. A. Martins, A. B. Lambe, Multidisciplinary design optimization: A survey of architectures, *AIAA Journal* 51 (9) (2013) 2049–2075. doi:10.2514/1.J051895. 2, 3

[35] J.-N. Walther, A.-A. Gastaldi, R. Maierl, A. Jungo, M. Zhang, Integration aspects of the collaborative aero-structural design of an unmanned aerial vehicle, *CEAS Aeronautical Journal* 11 (1) (2020) 217–227. doi:10.1007/s13272-019-00412-2. 2

[36] J.-H. Kim, T. Tsuchiya, Openvsp based aerodynamic design optimization tool building method and its application to tailless uav, in: Proceedings of the 33rd Congress of the International Council of the Aeronautical Sciences (ICAS), Stockholm, Sweden, 2022. 2, 32

[37] C. Parrott, S. Peddada, J. T. Allison, K. James, Machine learning surrogates for optimal 2d spatial packaging of interconnected systems with physics interactions (spi2), in: *AIAA AVIATION 2023 Forum*, American Institute of Aeronautics and Astronautics, 2023. doi:10.2514/6.2023-4375. 3

[38] L. Regenwetter, Y. A. Obaideh, F. Chiotti, I. Lykourentzou, F. Ahmed, Bike-bench: A bicycle design benchmark for generative models with objectives and constraints (2025). doi:10.48550/arXiv.2508.00830. 3, 6

[39] A. Berzins, A. Radler, E. Volkmann, S. Sanokowski, S. Hochreiter, J. Brandstetter, Geometry-informed neural networks (2025). doi:10.48550/arXiv.2402.14009. 3

[40] F. Felten, G. Apaza, G. Bräunlich, C. Diniz, X. Dong, A. Drake, M. Habibi, N. J. Hoffman, M. Keeler, S. Massoudi, F. G. VanGessel, M. Fuge, Engibench: A framework for data-driven engineering design research (2025). doi:10.48550/arXiv.2508.00831. 3

[41] I. M. Kroo, Mdo for large-scale design, in: *Multidisciplinary Design Optimization: State of the Art*, SIAM, Philadelphia, PA, 1997, pp. 22–44. 3

[42] W. Chen, M. Fuge, Synthesizing designs with interpart dependencies using hierarchical generative adversarial networks, *Journal of Mechanical Design* 141 (11) (2019). doi:10.1115/1.4044076. 3

[43] S. Dong, L. Ding, X. Chen, Y. Li, Y. Wang, Y. Wang, Q. Wang, J. Kim, C. Gao, Z. Huang, Z. Wang, T. Xue, D. Xu, From one to more: Contextual part latents for 3d generation, in: *Proceedings of the IEEE/CVF International Conference on Computer Vision (ICCV)*, 2025. doi:10.48550/arXiv.2507.08772. 3

[44] N. Talabot, O. Clerc, A. C. Demirtas, A. Goujon, H. Le, D. Oner, P. Fua, PartSDF: Part-based implicit neural representation for composite 3D shape parametrization and optimization, arXiv preprint arXiv:2502.12985 (2025). doi:10.48550/arXiv.2502.12985. 3

[45] L. Regenwetter, G. Giannone, A. Srivastava, D. Gutfreund, F. Ahmed, Constraining generative models for engineering design with negative data, *Transactions on Machine Learning Research* (2024). doi:10.48550/arXiv.2306.15166. 3, 5, 32

[46] M. Elfeki, C. Couplie, M. Riviere, M. Elhoseiny, GDPP: Learning diverse generations using determinantal point processes, in: *Proceedings of the 36th International Conference on Machine Learning*, Vol. 97 of *Proceedings of Machine Learning Research*, PMLR, 2019, pp. 1774–1783. doi:10.48550/arXiv.1812.00068. 3, 28

[47] W. Chen, F. Ahmed, Padgan: Learning to generate high-quality novel designs, *Journal of Mechanical Design* 143 (031703) (2020). doi:10.1115/1.4048626. 3, 17, 28

[48] W. Chen, F. Ahmed, Mo-padgan: Reparameterizing engineering designs for augmented multi-objective optimization, *Applied Soft Computing* 113 (2021). doi:10.1016/j.asoc.2021.107909. 3

[49] K. Deb, A. Pratap, S. Agarwal, T. Meyarivan, A fast and elitist multiobjective genetic algorithm: Nsga-ii 6 (2) 182–197. doi:10.1109/4235.996017. 3

[50] D. Mahapatra, V. Rajan, Multi-task learning with user preferences: Gradient descent with controlled ascent in pareto optimization, in: *International Conference on Machine Learning*, PMLR, 2020, pp. 6597–6607. 3

[51] A. Chandrasekhar, K. Suresh, Tounn: topology optimization using neural networks, *Structural and Multidisciplinary Optimization* 63 (3) (2021) 1135–1149. 3

[52] A. Joglekar, H. Chen, L. B. Kara, Dmf-tonn: direct mesh-free topology optimization using neural networks, *Engineering with Computers* 40 (4) (2024) 2227–2240. 3

[53] S. Basir, I. Senocak, An adaptive augmented lagrangian method for training physics and equality constrained artificial neural networks (2023). doi:10.48550/arXiv.2306.04904. 3

[54] T. D. Economou, F. Palacios, S. R. Copeland, T. W. Lukaczyk, J. J. Alonso, Su2: An open-source suite for multiphysics simulation and design, *AIAA Journal* 54 (3) (2016) 828–846. doi:10.2514/1.J053813. 3

[55] P. He, C. A. Mader, J. R. Martins, K. J. Maki, An aero-dynamic design optimization framework using a discrete adjoint approach with openfoam 168 285–303. doi:10.1016/j.compfluid.2018.04.012. 3

[56] P. He, C. A. Mader, J. R. R. A. Martins, K. J. Maki, Dafoam: An open-source adjoint framework for multi-disciplinary design optimization with openfoam 58 (3) 1304–1319. doi:10.2514/1.J058853. 3

[57] T. Xue, S. Liao, Z. Gan, C. Park, X. Xie, W. K. Liu, J. Cao, Jax-fem: A differentiable gpu-accelerated 3d finite element solver for automatic inverse design and mechanistic data science, *Computer Physics Communications* 291 (2023). doi:10.1016/j.cpc.2023.108802. 3

[58] F. L. Ferretti, D. Ferigo, C. Sartore, A. Croci, O. G. Younis, S. Traversaro, D. Pucci, Hardware-accelerated morphology optimization via physically consistent differentiable simulation (2025). URL <https://github.com/ami-iit/jaxsim> 3

[59] E. Todorov, T. Erez, Y. Tassa, Mujoco: A physics engine for model-based control, in: *2012 IEEE/RSJ International Conference on Intelligent Robots and Systems*, IEEE, 2012, pp. 5026–5033. doi:10.1109/IROS.2012.6386109. 3

[60] M. Banović, O. Mykhaskiv, S. Auriemma, A. Walther, H. Legrand, J.-D. Müller, Algorithmic differentiation of the open cascade technology cad kernel and its coupling with an adjoint cfd solver, *Optimization Methods and Software* 33 (4-6) (2018) 813–828. doi:10.1080/10556788.2018.1431235. 3

[61] M. Banović, T. Hafemann, A. Stück, Algorithmic differentiation of the pythonocc geometric modeling library, in: *ECCOMAS Congress 2024 (9th European Congress on Computational Methods in Applied Sciences and Engineering)*, Lisbon, Portugal, 2024. doi:10.23967/eccomas.2024.197. 3

[62] D. Cascaval, M. Shalah, P. Quinn, R. Bodik, M. Agrawala, A. Schulz, Differentiable 3d cad programs for bidirectional editing, in: *Computer Graphics Forum*, Vol. 41, Wiley Online Library, 2022, pp. 309–323. doi:10.1111/cgf.14476. 3

[63] A. Deva Prasad, A. Balu, H. Shah, S. Sarkar, C. Hegde, A. Krishnamurthy, Nurbs-diff: A differentiable programming module for nurbs, *Computer-Aided Design* 146 (2022). doi:10.1016/j.cad.2022.103199. 3

[64] J. J. Park, P. R. Florence, J. Straub, R. A. Newcombe, S. Lovegrove, Deep sdf: Learning continuous signed distance functions for shape representation, in: *Proceedings of the IEEE/CVF Conference on Computer Vision and Pattern Recognition (CVPR)*, 2019, pp. 165–174. doi:10.1109/CVPR.2019.00025. 4

[65] Z. Hao, H. Averbuch-Elor, N. Snavely, S. J. Belongie, Dualsdf: Semantic shape manipulation using a two-level representation, in: *Proceedings of the IEEE/CVF Conference on Computer Vision and Pattern Recognition (CVPR)*, 2020, pp. 7628–7638. doi:10.1109/CVPR42600.2020.00765. 4

[66] S. Vasu, N. Talabot, A. Lukoianov, P. Baqué, J. Donier, P. Fua, Hybridsdf: Combining deep implicit shapes and geometric primitives for 3d shape representation and manipulation, in: 2022 International Conference on 3D Vision (3DV), 2022, pp. 617–626. doi:10.1109/3DV57658.2022.00072. 4

[67] A. Heyrani Nobari, W. Chen, F. Ahmed, Range-gan: Design synthesis under constraints using conditional generative adversarial networks, *Journal of Mechanical Design* (2021) 1–16doi:10.1115/1.4052442. 4

[68] A. D. Cobb, A. Roy, D. Elenius, S. Jha, Design of unmanned air vehicles using transformer surrogate models (2022). doi:10.48550/arXiv.2211.08138. 4

[69] N. Sung, S. Spreizer, M. Elrefaie, K. Samuel, M. C. Jones, F. Ahmed, Blendednet: A blended wing body aircraft dataset and surrogate model for aerodynamic predictions (2025). doi:10.7910/DVN/VJT9EP. 4

[70] J. Feydy, T. Séjourné, F.-X. Vialard, S.-i. Amari, A. Trouvé, G. Peyré, Interpolating between optimal transport and mmd using sinkhorn divergences, in: The 22nd International Conference on Artificial Intelligence and Statistics, PMLR, 2019, pp. 2681–2690. doi:10.48550/arXiv.1810.08278. 4, 32

[71] A. Paszke, S. Gross, F. Massa, A. Lerer, J. Bradbury, G. Chanan, T. Killeen, Z. Lin, N. Gimelshein, L. Antiga, A. Desmaison, A. Kopf, E. Yang, Z. DeVito, M. Raison, A. Tejani, S. Chilamkurthy, B. Steiner, L. Fang, J. Bai, S. Chintala, Pytorch: An imperative style, high-performance deep learning library, in: Proceedings of the 33rd International Conference on Neural Information Processing Systems. 4, 33

[72] B. Letham, R. Calandra, A. Rai, E. Bakshy, Re-examining linear embeddings for high-dimensional bayesian optimization, *Advances in Neural Information Processing Systems* 33 (2020) 1546–1558. doi:10.48550/arXiv.2001.11659. 4, 29

[73] D. Eriksson, M. Jankowiak, High-dimensional bayesian optimization with sparse axis-aligned subspaces, in: Uncertainty in Artificial Intelligence, PMLR, 2021, pp. 493–503. doi:10.48550/arXiv.2103.00349. 4, 29

[74] D. Eriksson, M. Pearce, J. Gardner, R. D. Turner, M. Poloczek, Scalable global optimization via local bayesian optimization, *Advances in Neural Information Processing Systems* 32 (2019). doi:10.48550/arXiv.1910.01739. 4, 29

[75] J. Blank, K. Deb, pymoo: Multi-objective optimization in python, *IEEE Access* 8 (2020) 89497–89509. doi:10.1109/ACCESS.2020.2990567. 6, 11

[76] X. Zhang, L. Zhao, Y. Yu, X. Lin, Y. Chen, H. Zhao, Q. Zhang, Libmoon: A gradient-based multi-objective optimization library in pytorch, *Advances in Neural Information Processing Systems* 37 (2024) 2026–2044. doi:10.48550/arXiv.2409.02969. 6

[77] M. Olson, E. Santorella, L. C. Tiao, S. Cakmak, M. Garrard, S. Daulton, Z. J. Lin, S. Ament, B. Beckerman, E. Onofrey, P. Igusti, C. Lara, B. Letham, C. Cardoso, S. S. Shen, A. C. Lin, M. Grange, E. Kashtelyan, D. Eriksson, M. Balandat, E. Bakshy, Ax: A platform for adaptive experimentation, in: AutoML 2025 ABCD Track, 2025. URL <https://ax.dev/> 32

[78] S. F. Hoerner, *Fluid-Dynamic Drag: Practical Information on Aerodynamic Drag and Hydrodynamic Resistance*, Hoerner Fluid Dynamics, Bricktown, NJ, 1965. 32

Appendix A. DF-GLUE Hyperparameters

Table A.5 lists the specific hyperparameters used for DF-GLUE across the different experiments presented in this work. The hyperparameters include the random seeds, sampling count, numerical tolerance, DPP kernel width σ , latent dimension size $\dim(\zeta)$, and the loss weights for DPP diversity terms (λ_{DPP}), mutual information (λ_{MI}), and performance optimization (λ_{perf}). Where weights are annealed during training, the schedule is denoted as start → end.

Appendix B. Subsystem Model Specifications

Table B.6 provides a detailed comparison of the three subsystem models.

Appendix B.1. Wing Model

The wing model builds on existing work by Chen and Fuge [2]. The outer conditional generator takes a latent code $z \in \mathbb{R}^2$ together with flight requirements (velocity V , altitude h , wing lift requirement L_{req}) and produces the corresponding wing parameters. These parameters are chord c , span b , and coefficient of lift C_L . Training proceeds in two distinct phases: physics-based losses are applied during the initial epochs 0 to 150, after which diversity objectives are gradually introduced. A Q-network provides mutual information regularization to encourage meaningful latent representations. The resulting model satisfies lift requirements across a range of flight conditions while maintaining aerodynamic validity. The outer wing model provides conditions (Mach number, Reynolds number based on chord and velocity, and coefficient of lift C_L) to an inner airfoil model (BézierGAN). The inner airfoil model generates an airfoil shape (coordinate points and angle of attack). The airfoil is then scaled to the chord c and extruded linearly along the span b .

Appendix B.2. Airfoil Model

For more information, please refer to [2]. We use the CE-BGAN architecture trained on 995 optimized airfoil samples. The model maps 3 conditions (Mach number, Reynolds number, and coefficient of lift C_L) to 192×2 points (x, z coordinates of airfoil surface) and angle of attack. The wing model is trained

Table A.5: DF-GLUE hyperparameters for the different experiments presented in the paper.

	Opt-Feas-Div (Figure 6)	Opt-Feas-Compute (Figure 7)	SN Abl. (Table 3)	Mode Coll. Abl. (Table 4)
dim(ζ)	4	4	2	2
Sampling Mode	Latin Hypercube	Latin Hypercube	Latin Hypercube	Latin Hypercube
Batch Size	1296	1296	1296	1296
Learning Rate	0.001	0.001	0.001	0.001
LR Decay Multiplier	-	-	0.9985	0.9985
ALM Mode	Pooled	Pooled	Hypercube	Hypercube
ALM α	0.9	0.9	0.9	0.9
ALM C_{cap}	500	500	-	-
ALM γ	0.005	0.005	0.005	0.005
λ_{perf}	Figure 6	0.1	0.25	0.25
$\lambda_{\text{DPP},X}$	Figure 6	0	0	0
λ_{DPP,z_F}	0	0	0.2	0.2
λ_{DPP,z_W}	0	0	0	0.1
λ_{DPP,z_I}	0	0	0	$30 \rightarrow 0.4$
λ_{MI}	0	0	$8 \rightarrow 0.2$	$8 \rightarrow 0.2$

to map (z_W, L, eq) to appropriate airfoil parameters (C_l, Re, Ma) given environmental conditions (altitude, velocity). The airfoil is then scaled using chord c and extruded linearly along the span b . These (b, c) are also outputs of the wing model.

Appendix B.3. Fuselage Model

We employ a custom VAE trained on parametric fuselage geometries, as illustrated in Figure B.13. The VAE maps a four-dimensional latent code $z \in \mathbb{R}^4$ to 15 geometric parameters. Note that the full fuselage parametrization contains additional parameters that are fixed for simplicity (see Figure B.13 for an overview). The training data consists of 551 valid designs selected from 200k candidates through rejection sampling (convexity, self-intersection, etc.), yielding a 0.28% acceptance rate. We employ SN to ensure smooth $z_F \rightarrow x_F$ mappings and incorporate a minimum volume loss [20] to impose structure on the latent space. The resulting model performs unconditional generation with smooth interpolation properties.

Figure B.12 illustrates the effect of the minimum volume loss on the latent space organization. The loss promotes disentanglement, resulting in principal axes that correspond to distinct geometric features: the first axis controls tail dihedral, the second tail location, the third main section width, and the fourth isotropic scaling. While other features (e.g., nose shape, front dihedral) also vary, the minimum volume loss effectively aligns the most dominant variations with the latent axes. Note that we fix the latent dimension to four without extensive dimensionality analysis.

Appendix B.4. Internals Component Placement Model

We use a custom autoregressive model that serves as a simple placeholder for more detailed component models. The autoregressive model takes $z \in \mathbb{R}^4$ and volumes $\{V_i\}$ and produces box parameters $\{(\ell_i, w_i, h_i, x_i, y_i, z_i)\}_i$. The model is trained with variable sequence length, but for simplicity during optimization and GLUE model training we fix the sequence length to three boxes. An embedding network processes placement history for

spatial reasoning. We employ data-free training with geometric losses. These are: overlap, accurate volume (constraint to match each box’s volume to the conditional requirement), compactness of the layout, and adjacent diversity (encouraging diverse configurations). An auxiliary network provides mutual information regularization. The inference procedure includes a cleanup step: after initial box prediction, a gradient descent procedure refines box positions to eliminate collisions and improve compactness. This cleanup step is crucial for ensuring physically valid configurations. Additionally, for the sake of simplicity, all boxes are placed with their centers at $y = 0$ and are symmetric with regards to the xz plane.

In the long term, we are interested in more complex subsystem models for internal components and wish to build upon this simple box-based model.

Appendix B.5. Loss Formulations

Appendix B.5.1. Wing Model

The total loss for the wing model is given by:

$$\mathcal{L}_{\text{wing}} = \lambda_{\text{lift}} \mathcal{L}_{\text{lift}} + \lambda_{\text{Re}} \mathcal{L}_{\text{Re}} + \lambda_{\text{DPP}} \mathcal{L}_{\text{PA-DPP}} + \lambda_{\text{MutualInformation(MI)}} \mathcal{L}_{\text{MI}} \quad (\text{B.1})$$

The lift accuracy loss is given by:

$$\mathcal{L}_{\text{lift}} = \text{MSE} \left(\frac{L}{10^4}, \frac{L_{\text{req}}}{10^4} \right), \quad L = \frac{1}{2} \rho V^2 C_L c b \quad (\text{B.2})$$

where $C_L = C_\ell / (1 + C_\ell / (\pi e \cdot \text{AR}))$, $\text{AR} = b/c$, $e = 0.8$ (Oswald efficiency factor), and $\lambda_{\text{lift}} = 400$.

To ensure that the Airfoil model ([2]) is only used with Reynolds numbers within the training range, we employ a penalty to enforce wing model outputs to be within this range.

$$\mathcal{L}_{\text{Re}} \propto \sum_{i=1}^B \frac{\text{ReLU}(\text{Re}_{\min} - \text{Re}_i) + \text{ReLU}(\text{Re}_i - \text{Re}_{\max})}{B} \quad (\text{B.3})$$

where $\text{Re} = \rho V c / \mu$ with $\text{Re} \in [10^5, 10^8]$. Ramp schedule: $\lambda_{\text{Re}} = 1$ for epochs < 150 , linear ramp to 1000 over epochs 150–200.



Figure B.11: Wing model sample generation. The wing model maps flight requirements (L_{req}, V, h) and latent code z_W to wing parameters (c, b, C_L). It also outputs conditions (Ma, Re, Cl) for the inner airfoil model, which generates the corresponding airfoil shape and angle of attack. The airfoil is then scaled by chord c and extruded along span b .

The performance-augmented DPP loss [47] is given by:

$$\mathcal{L}_{PA-DPP} = -\log \det(L), \quad L = K \odot (q q^\top) \quad (B.4)$$

where the similarity kernel is defined as $K_{ij} = \exp\left(-\frac{\|x_i - x_j\|_2^2}{2\sigma^2}\right)$ with $\sigma = 0.1$, applied to normalized wing parameters $x = (c, b, C_L) \in [0, 1]^3$. The quality score is computed as $q_i = (L/D)_i^2/m_i^2$, where $L/D = \pi(b/c)e/C_\ell$ represents the lift-to-drag ratio and $m = C_{mw}M_{root}/g + C_{ar}b$ represents the wing mass with coefficients $C_{mw} = 4 \times 10^{-4}$ and $C_{ar} = 1$. We use a ramp

schedule: $\lambda_{DPP} = 0$ for epochs < 150 , linear ramp to 5×10^{-5} over epochs 150–200.

To enforce disentanglement for the wing model, we employ a mutual information loss. This is given by:

$$\mathcal{L}_{MI} = \text{MSE}(z_{\text{pred}}, z), \quad z_{\text{pred}} = Q(x, V, h, L_{\text{req}}) \quad (B.5)$$

where Q is a Q-Network trained to invert the generator mapping, with $\lambda_{MI} = 0.2$.

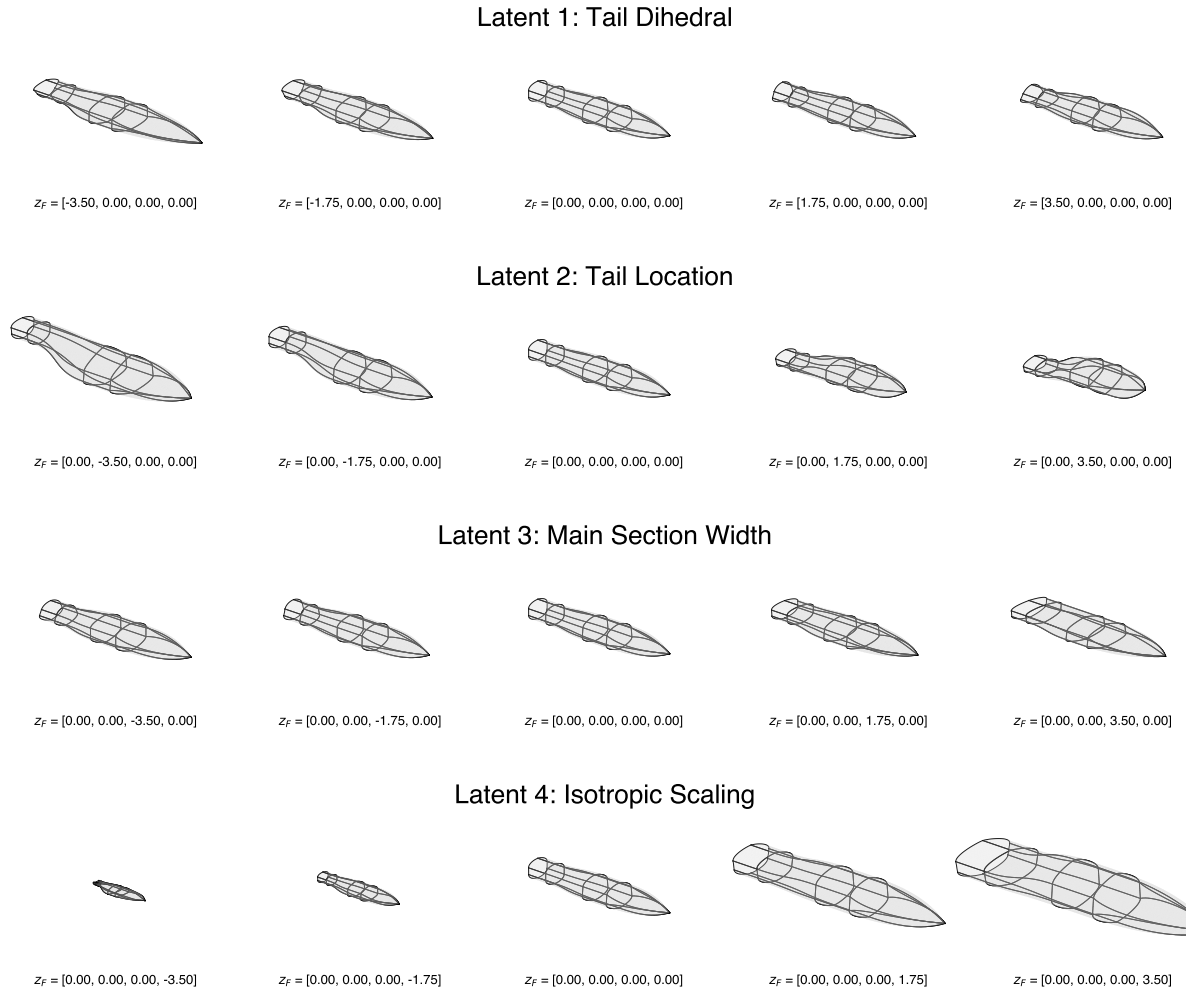


Figure B.12: Fuselage latent space sweep illustrating disentanglement. Each row shows variations along a single latent axis z_i while holding others fixed at zero.

Appendix B.5.2. Fuselage Model

The total loss for the fuselage model is given by:

$$\mathcal{L}_{\text{fuselage}} = \mathcal{L}_{\text{recon}} + \lambda_{\text{KL}} \mathcal{L}_{\text{KL}} + \lambda_{\text{LV}} \mathcal{L}_{\text{LV}} \quad (\text{B.6})$$

The reconstruction loss is given by:

$$\mathcal{L}_{\text{recon}} = \text{MSE}(\mathbf{x}_{\text{recon}}, \mathbf{x}) \quad (\text{B.7})$$

The KL divergence loss is given by:

$$\mathcal{L}_{\text{KL}} = -\frac{1}{2B} \sum_{i=1}^B \sum_{j=1}^{d_z} \left(1 + \log(\sigma_{ij}^2) - \mu_{ij}^2 - \sigma_{ij}^2 \right) \quad (\text{B.8})$$

where μ, σ^2 are encoder outputs, $d_z = 4$ is the latent dimension, B is the batch size, and $\lambda_{\text{KL}} = 0.04$.

The least volume loss is used for disentanglement of the latent space. It is given by:

$$\mathcal{L}_{\text{LV}} = \exp \left(\frac{1}{d_z} \sum_{j=1}^{d_z} \log(\text{std}(z_j) + \eta) \right), \quad \eta = 10^{-4} \quad (\text{B.9})$$

where $\text{std}(z_j)$ is the standard deviation of the j -th latent dimension across the batch, and $\lambda_{\text{LV}} = 0.12$. Please note that this loss is used in conjunction with SN and is in competition with the KL divergence.

Appendix B.5.3. Internals Model

The total loss for the internals model is given by:

$$\mathcal{L}_{\text{internals}} = \lambda_{\text{overlap}} \mathcal{L}_{\text{overlap}} + \lambda_{\text{volume}} \mathcal{L}_{\text{volume}} + \lambda_{\text{compact}} \mathcal{L}_{\text{compact}} \quad (\text{B.10})$$

$$+ \lambda_{\text{LDV}} \mathcal{L}_{\text{LDV}} + \lambda_{\text{AR-DPP}} \mathcal{L}_{\text{AR-DPP}} + \lambda_{\text{MI}} \mathcal{L}_{\text{MI}} \quad (\text{B.11})$$

The overlap penalty is given by:

$$\mathcal{L}_{\text{overlap}} = \frac{1}{B} \sum_{i=1}^B \frac{\|\mathbf{A}_i^{\text{overlap}}\|_2}{\|\mathbf{V}_i\|_2} \quad (\text{B.12})$$

where $\mathbf{A}_i^{\text{overlap}}$ is the overlap matrix and \mathbf{V}_i are the box volumes for sample i . Ramp schedule: $\lambda_{\text{overlap}} = 4$ for epochs < 500 , linear ramp to 20 over epochs 500–1500.

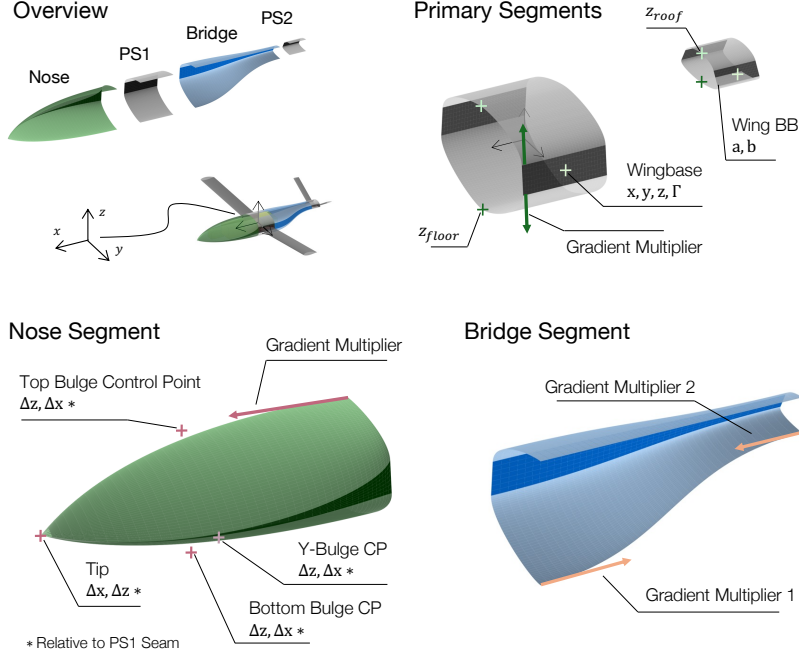


Figure B.13: Fuselage parametrization overview showing primary segments, bridge, and nose components. The nose and bridge segments consist of three bicubic Bézier surface patches each. The primary segments consist of three linearly extruded cubic Bézier curves. The middle primary segment Bézier curves are perfectly straight and act as the wing interfaces.

The volume deficit loss is given by:

$$\mathcal{L}_{\text{volume}} = \left\| \frac{\mathbf{V}_{\text{actual}} - \mathbf{V}_{\text{target}}}{\mathbf{V}_{\text{target}}} \right\|_2 \quad (\text{B.13})$$

Ramp schedule: $\lambda_{\text{volume}} = 5$ for epochs < 500 , linear ramp to 10 over epochs 500–1500.

The compactness loss is given by:

$$\mathcal{L}_{\text{compact}} = 0.6 \cdot \text{slenderness} + 0.4 \cdot \text{fill}^{-1} \quad (\text{B.14})$$

where slenderness is defined as $\text{slenderness} = \sqrt{A_{\text{frontal}} / \sqrt{A_{\text{side}} \cdot A_{\text{top}}}}$ and the inverse fill ratio is computed as $\text{fill}^{-1} = V_{\text{bounding}} / \sum_i V_i$. Ramp schedule: $\lambda_{\text{compact}} = 2$ for epochs < 500 , linear ramp to 4 over epochs 500–1500.

The layout diversity via adjacency loss is given by:

$$\mathcal{L}_{\text{LDV}} = \mathcal{L}_{\text{DPP}}(\mathbf{A}_x) + \mathcal{L}_{\text{DPP}}(\mathbf{A}_z), \quad (\text{B.15})$$

$$\text{where } \mathcal{L}_{\text{DPP}}(\mathbf{A}) = -\frac{1}{B} \log \det(\mathbf{K}_A) \quad (\text{B.16})$$

where $\mathbf{A}_x, \mathbf{A}_z$ are adjacency matrices in x and z directions, $K_{A,ij} = \exp(-\|\text{vec}(\mathbf{A}_i) - \text{vec}(\mathbf{A}_j)\|_2^2 / (2\sigma^2))$ with $\sigma = 1$, and $\lambda_{\text{LDV}} = 0.5$.

The aspect ratio diversity loss is given by:

$$\mathcal{L}_{\text{AR-DPP}} = -\frac{1}{B} \log \det(\mathbf{K}_{\text{AR}}), \quad \text{AR} = \log \left[\frac{w}{\ell}, \frac{h}{\ell} \right] \quad (\text{B.17})$$

where $K_{\text{AR},ij} = \exp(-\|\text{vec}(\text{AR}_i) - \text{vec}(\text{AR}_j)\|_2^2 / (2\sigma^2))$ with $\sigma = 1$. Ramp schedule: $\lambda_{\text{AR-DPP}} = 4$ for epochs < 500 , linear ramp

to 1 over epochs 500–1500 (decreasing). This loss is used to encourage boxes with varying aspect ratios.

The mutual information loss is given by:

$$\mathcal{L}_{\text{MI}} = -\frac{1}{B} \sum_{i=1}^B \log \frac{\exp(\mathbf{z}_i^\top \hat{\mathbf{z}}_i / \tau)}{\sum_{j=1}^B \exp(\mathbf{z}_i^\top \hat{\mathbf{z}}_j / \tau)} \quad (\text{B.18})$$

where $\hat{\mathbf{z}}_i$ is the predicted latent code from the auxiliary predictor, $\tau = 0.1$ is the temperature, and $\lambda_{\text{MI}} = 0.1$.

Appendix B.6. Architecture Details

Appendix B.6.1. Wing Model

The wing model consists of two networks: a generator $G : (z, V, h, L_{\text{req}}) \in \mathbb{R}^5 \rightarrow (c, b, C_L) \in \mathbb{R}^3$ and a Q-Network for mutual information regularization mapping $(c, b, C_L, V, h, L_{\text{req}}) \in \mathbb{R}^6 \rightarrow z \in \mathbb{R}^2$. Both networks are implemented as 4-layer MLPs with hidden size 32 and ReLU activations. Input and output normalization is performed via registered buffers using affine scaling to the range $[-1, 1]$. Training proceeds with alternating updates, first updating the Q-Network and then the generator.

Appendix B.6.2. Fuselage Model

The fuselage VAE comprises an encoder mapping $\mathbf{x} \in \mathbb{R}^{15} \rightarrow (\mu, \log \sigma^2) \in \mathbb{R}^4 \times \mathbb{R}^4$ and a decoder mapping $\mathbf{z} \in \mathbb{R}^4 \rightarrow \mathbf{x} \in \mathbb{R}^{15}$. The architecture employs a main path with layer sizes 128, 64, and 32, augmented with skip connections from dimension 15 to 32 and from dimension 4 to 15. SN is applied to most layers to ensure smoothness in the latent-to-parameter mapping. Data normalization is performed using z-score standardization: $(\mathbf{x} - \mu_{\text{train}}) / \sigma_{\text{train}}$.

Table B.6: Detailed comparison of subsystem models for wing, fuselage, and box arrangement (internals).

Aspect	Wing	Fuselage	Internals
Model Type	Conditional Generator	VAE	Autoregressive MLP
Latent Dim	2	4	4
Output Dim	3	15	$6 \times \text{seq_len}$
Training Epochs	1,500	1,000	2,500
Batch Size	256	128	256
Learning Rate	$10^{-3} \rightarrow 5 \times 10^{-4}$	2×10^{-4}	5×10^{-4}
Loss 1	Lift Accuracy ($\lambda = 400$)	Reconstruction Mean Squared Error (MSE)	Overlap Penalty ($\lambda : 4 \rightarrow 20$)
Loss 2	Reynolds Constraint ($\lambda : 1 \rightarrow 1000$)	Kullback-Leibler (KL) Divergence ($\lambda = 0.04$)	Volume Deficit ($\lambda : 5 \rightarrow 10$)
Loss 3	Performance-Augmented Determinantal Point Process (PA-DPP) ($\lambda : 0 \rightarrow 5 \times 10^{-5}$)	Least Volume ($\lambda = 0.12$)	Compactness ($\lambda : 2 \rightarrow 4$)
Loss 4	Mutual Information ($\lambda = 0.2$)	—	Layout Diversity (DPP) ($\lambda = 0.5$)
Loss 5	—	—	Aspect Ratio Diversity ($\lambda : 4 \rightarrow 1$)
Loss 6	—	—	Mutual Information ($\lambda = 0.1$)
Total Active Losses	4	3	6
Ramp Schedule	Yes (epoch 150)	No	Yes (epoch 500–1500)
Training Data	Synthetic (online)	Filtered 200k → 551	Synthetic (online)

Appendix B.6.3. Internals Model

The internals model employs an autoregressive architecture with three key components: an embedding network $\mathbf{b}_i \in \mathbb{R}^6 \rightarrow \mathbf{e}_i \in \mathbb{R}^{1024}$ that encodes box parameters, a box generator $(\mathbf{e}_{\text{cum}}, \mathbf{z}, \text{seq_len}, V_i) \in \mathbb{R}^{1029} \rightarrow \mathbf{b}_i \in \mathbb{R}^6$ that produces the next box, and an auxiliary predictor $(\mathbf{x}_i, \mathbf{e}_{\text{cum}}, \text{seq_len}) \in \mathbb{R}^{1028} \rightarrow \Delta \mathbf{z}_i \in \mathbb{R}^4$ for mutual information regularization. The model operates autoregressively, updating the cumulative embedding as $\mathbf{e}_{\text{cum}} \leftarrow \mathbf{e}_{\text{cum}} + \mathbf{e}_i$ after generating each box. The final latent prediction is computed as $\hat{\mathbf{z}} = \sum_{i=1}^N \Delta \mathbf{z}_i$. All MLPs in this architecture use LeakyReLU activations.

Appendix B.7. Training Strategies

Appendix B.7.1. Wing Model

The wing model is trained using a two-stage learning rate schedule: 10^{-3} for epochs 0 to 150, then 5×10^{-4} for subsequent epochs. Diversity enforcement is introduced at epoch 150, allowing the model to first converge on physics-based objectives. Each epoch processes 12 batches of 256 samples, totaling 3,072 samples per epoch. The Reynolds constraint and DPP loss ramps are synchronized with the learning rate transition. Training uses random seed 42 and the Adam optimizer with default PyTorch parameters ($\beta_1 = 0.9, \beta_2 = 0.999, \epsilon = 10^{-8}$).

Appendix B.7.2. Fuselage Model

The fuselage model uses a constant learning rate of 2×10^{-4} with constant loss weights throughout training (no ramping). The 551 valid designs are split 80%/20% into training and test sets. Test set evaluation is performed every epoch for monitoring purposes. Training employs random seed 5 and the Adam optimizer with default PyTorch parameters ($\beta_1 = 0.9, \beta_2 = 0.999, \epsilon = 10^{-8}$).

Appendix B.7.3. Internals Model

The internals model is trained with a constant learning rate of 5×10^{-4} over three distinct phases. Phase one (epochs 0 to 500) focuses on initial convergence with lower penalty weights. Phase two (epochs 500 to 1500) implements progressive ramping with linear weight increases. Phase three (epochs 1500 to 2500) performs fine-tuning under maximum constraint penalties. All sequence lengths (1 to 3 boxes) are trained simultaneously, with random target volumes sampled per epoch to ensure generalization. Training uses random seeds torch=42 and numpy=5, and employs the Adam optimizer with default PyTorch parameters ($\beta_1 = 0.9, \beta_2 = 0.999, \epsilon = 10^{-8}$).

Appendix B.8. Dataset Generation: Fuselage

The fuselage dataset is generated via rejection sampling with extensive geometric validation. Beginning with 200,000 randomly sampled parameter sets, candidates undergo a multi-stage filtering process. Stage one performs preliminary checks on minimum and maximum dimensions, aspect ratios, and z-ordering. Stage two tests for self-intersection in the front and rear primary segments. Stage three checks for intersections with the symmetry plane. Stage four evaluates convexity, requiring all candidates to be convex. Stage five detects overlaps in bridge segments. Stage six validates smooth transitions between all adjacent segments. Following validation, accepted designs undergo post-validation scaling, where a random uniform factor from the range [0.15, 0.4] is applied to all length parameters. This rigorous process yields 551 valid designs from the initial 200,000 candidates, representing a 0.28% acceptance rate. The fuselage geometry comprises four interconnected components: front primary segment, rear primary segment, bridge, and nose.

Appendix C. DF-GLUE Architecture

We first detail the data free training architecture used in all experiments. We then ablate core components to isolate their effect and motivate the default architecture.

Appendix C.1. Default Architecture

Figure C.14 shows the architecture for DF-GLUE. A shared main block forms a 5 layer MLP of width 64. It maps the system level latent ζ to a Common Features (CF) vector. Dedicated MLP heads map CF to each subsystem latent and condition (z_i, c_i) and to placement variables $(x_{c,i})$ where required. The fuselage uses no placement head because it is fixed to the origin.

Latent and condition heads for the fuselage and wings 1 (front) and 2 (tail) use a single linear layer with tanh and sigmoid output activations, followed by per-dimension denormalization to the latent and condition scales of the frozen subsystem models. For these subsystems, the shared main block carries most coordination capacity.

Internals latent and placement heads use deeper MLPs with ReLU activations and one skip connection to mitigate vanishing gradients. This design supports gradient flow from internals objectives into the shared main block.

Wing placement heads use Wide Residual Blocks (WRBs) with ReLU activations as the basic unit. Each WRB forms a 3 layer MLP with dimensions $256 \rightarrow 512 \rightarrow 256$. A skip connection spans the full block. The default wing placement head stacks four WRBs in sequence, which provides skip connections at every block and maintains a direct skip path from the head input to the head output.

All head outputs use tanh or sigmoid to enforce bounded variables and then apply per-output denormalization scales.

The head depth for each subsystem results from manual tuning.

Appendix C.1.1. Weight Initialization

For the GLUE model, we use custom weight initialization for `nn.Sequential` modules. We iterate through layers, identify `nn.Linear` layers, and apply initialization based on the subsequent activation function.

For each `nn.Linear` layer with weight matrix $\mathbf{W} \in \mathbb{R}^{n_{\text{out}} \times n_{\text{in}}}$:

ReLU Activation. Kaiming Uniform initialization

$$W_{ij} \sim \mathcal{U}(-a, a), \quad \text{where } a = \sqrt{\frac{6}{n_{\text{in}}}} \quad (\text{C.1})$$

Tanh Activation. LeCun-like Normal initialization with more variance

$$W_{ij} \sim \mathcal{N}(0, \sigma^2), \quad \text{where } \sigma^2 = \frac{4}{n_{\text{in}}} \quad (\text{C.2})$$

Sigmoid Activation. LeCun-like Normal initialization with more variance

$$W_{ij} \sim \mathcal{N}(0, \sigma^2), \quad \text{where } \sigma^2 = \frac{4}{n_{\text{in}}} \quad (\text{C.3})$$

where n_{in} is the fan-in (number of input features).

Bias Initialization. All biases are initialized to zero:

$$b_i = 0 \quad \forall i \quad (\text{C.4})$$

This initialization only affects `nn.Linear` layers within `nn.Sequential` blocks. Skip connections and standalone linear layers defined outside sequential containers are not initialized by this function.

Appendix C.1.2. Wing Placement Optimizer

A dedicated optimizer for the wing placement heads as shown in Figure C.15 mitigates mode collapse, see Section 4.8.2. In the ablation, this mechanism is denoted as Inner Adam. Without this separation, gradients from C_{wx} and C_{di} backpropagate into the shared main block and drive collapse that prioritizes these constraints. The wing placement heads predict $x_{c,W1}$ and $x_{c,W2}$ from the CF vector produced by the main block. This separation prevents wing placement gradients from directly shaping fuselage and wing latent outputs.

Appendix C.2. Architecture Ablation

With our setup, the ability of DF-GLUE to learn constraints and optimize performance is sensitive to its architecture. We now ablate core components to isolate architectural factors that drive this sensitivity. We compare three alternatives against the default, which yields four architectures in total.

Architecture 1. This is the default and matches Figure C.14.

Architecture 2. Matches Architecture 1 but removes the custom initialization. For architecture 2, we use PyTorch default initialization for model weights and biases. This reduces initial weight variance. We find this significantly reduces the output variance. At the first training epoch, the output designs are virtually mode-collapsed.

Architecture 3. Shifts capacity from the shared main block into the fuselage and wing latent heads while keeping all other components identical to Architecture 1. Architecture 3 is shown in Figure C.16. The changes are marked in color. This ablation probes the capacity balance between the shared main block and subsystem heads.

Architecture 4. Modifies only the wing placement heads. It replaces the WRBs design with a deep sequential MLP with ReLU activations. It adds skip connections every sixth layer, which yields substantially fewer skip connections than Architecture 1. Architecture 4 is shown in Figure C.17.

Appendix C.2.1. Results

Figure C.18 reports training losses over 2500 epochs with $\lambda_{\text{opt}} = 0.1$ and $\lambda_{\text{DPP}} = 1$ using DPP on \mathcal{X} . Each architecture uses 10 seeds and the plots show mean curves only. We omit min and max ranges for visual clarity. Please see 2 for the full loss formulation. We use $\lambda_{\text{MI}} = 0$, and no subsystem-specific diversity enforcement ($\lambda_{\text{DPP},z_F} = \lambda_{\text{DPP},z_W} = \lambda_{\text{DPP},z_I} = 0$). We use hypercube ALM with $\gamma = 5 \cdot 10^{-3}$.

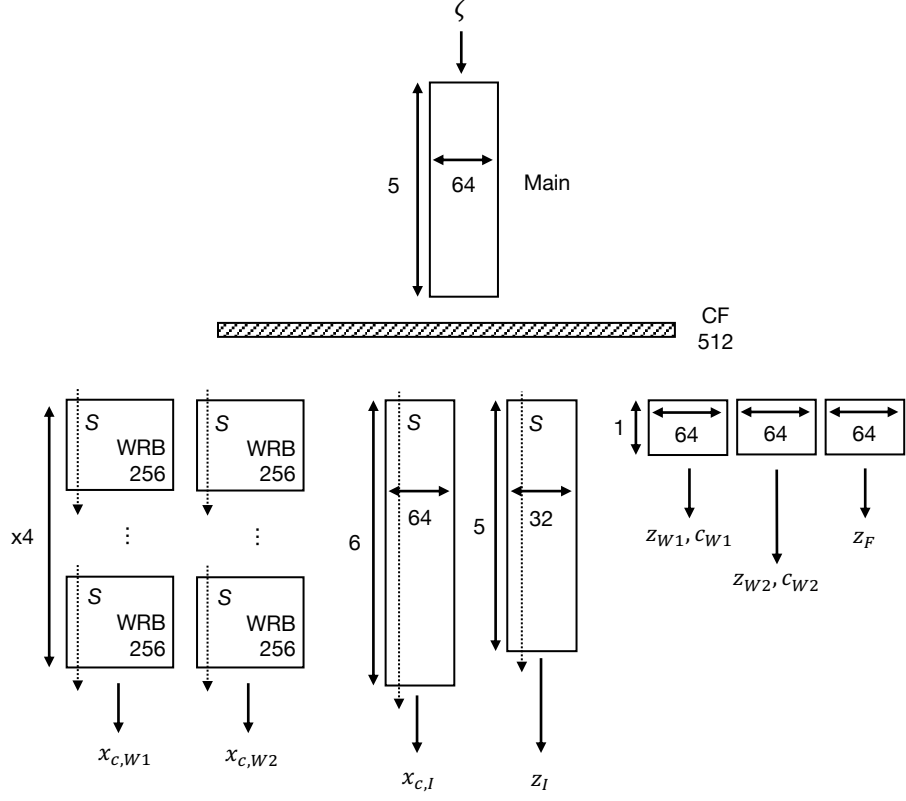


Figure C.14: DF-GLUE architecture used throughout this work (Architecture 1). MLP-based main block with subsystem latent and placement heads. Forward pass top-to-bottom, backward pass bottom-to-top.

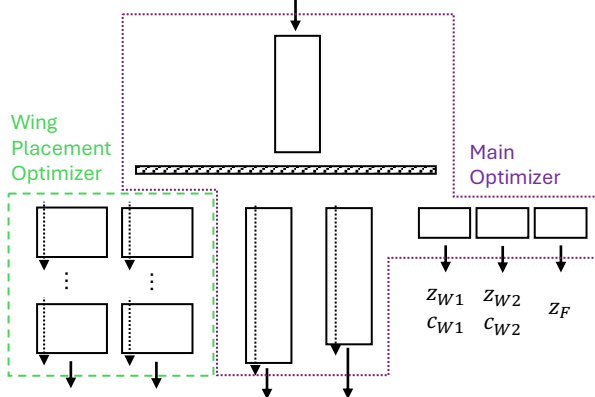


Figure C.15: Dedicated optimizer for wing placement block.

All experiments use the dedicated wing placement optimizer in Figure C.15. Figure C.19 summarizes feasibility and the performance-diversity trade-off across architectures. Shown are the single objective O_{mass} , diversity (DPP), and four constraints. C_{bb} is omitted, as it is by far the easiest of the constraints to satisfy.

Architecture 1 (blue) is the baseline and represents successful training. In Figure C.18, it achieves low loss across all constraints and objectives, which is indicative of adequate learning. As seen in Figure C.19, it maintains high feasibility even at high diversity while offering the best performance–diversity trade-off.

Architecture 2. Architecture 2 removes custom initialization. This degrades box placement and wing placement losses relative to Architecture 1. Consistent with this trend, Figure C.19 shows lower mean feasibility and a weaker performance–diversity trade-off. Architecture 2 also shows a distinct early training trajectory in which performance improves at initialization rather than initial degrading.

Architecture 3. Architecture 3 shifts capacity from the shared main block into the fuselage and wing latent heads. This degrades losses across most objectives and constraints in Figure C.18. It attains the lowest mean feasibility and the weakest performance–diversity trade-off as shown in Figure C.19.

Architecture 4. Architecture 4 replaces the WRBs wing placement heads with a deep sequential MLP with fewer skip connections. It matches Architecture 1 on C_{lift} and $C_{\text{box-pl}}$ (internals placement), but fails on wing placement constraints C_{wx} and C_{di} . In Figure C.19, its best seed reaches feasibility comparable to Architecture 1 while the mean feasibility and performance–diversity degrade. In practice, some seeds perform well, but a few runs remain at very high loss for C_{wx} and C_{di} and, on the log scale, dominate the mean. Thus, the high loss curves for C_{wx} and C_{di} in architecture 4 mainly reflect poor robustness across seeds, not uniformly poor performance. The same is also true for architecture 2.

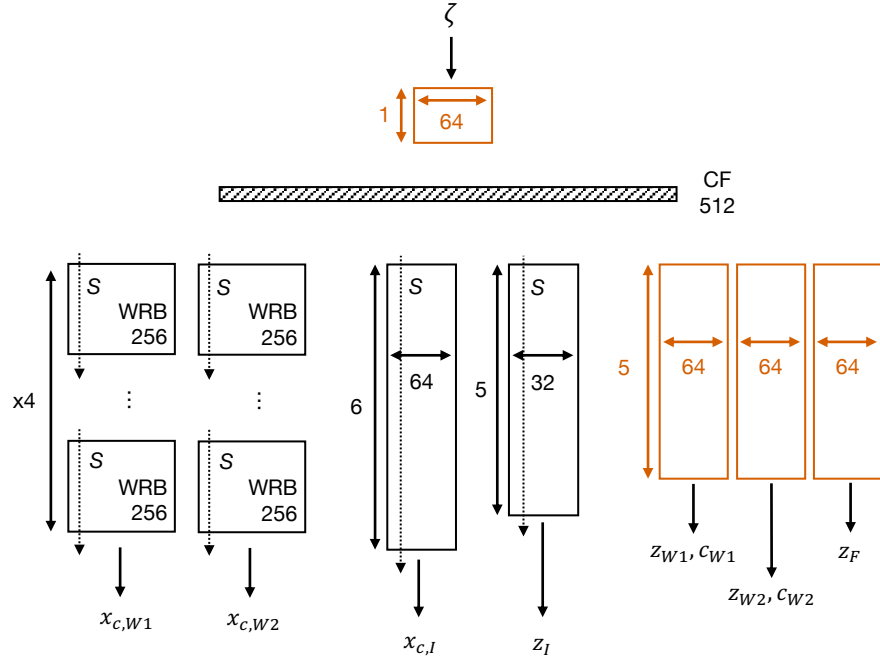


Figure C.16: DF-GLUE Architecture 3. Compared to default architecture 1, capacity is moved from the main block into the fuselage and wing latent heads while keeping the rest of the network unchanged.

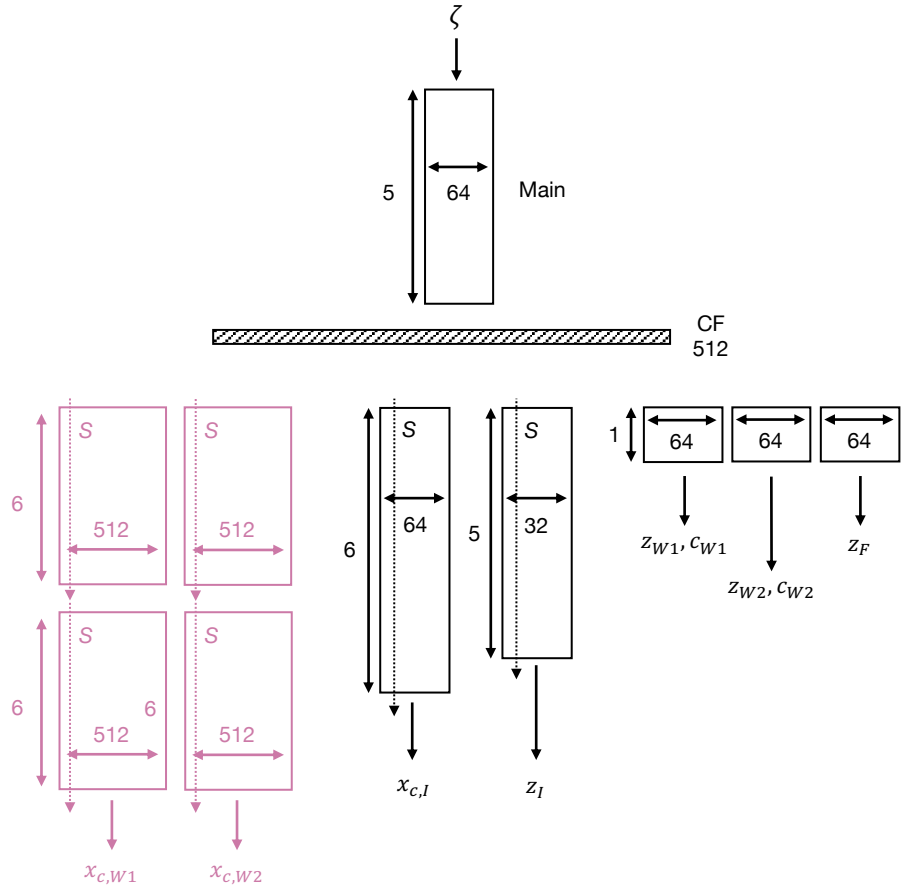


Figure C.17: DF-GLUE Architecture 4. Replaces the Wide Residual Blocks (WRB) wing placement heads of Architecture 1 with deep sequential MLP with fewer skip connections.

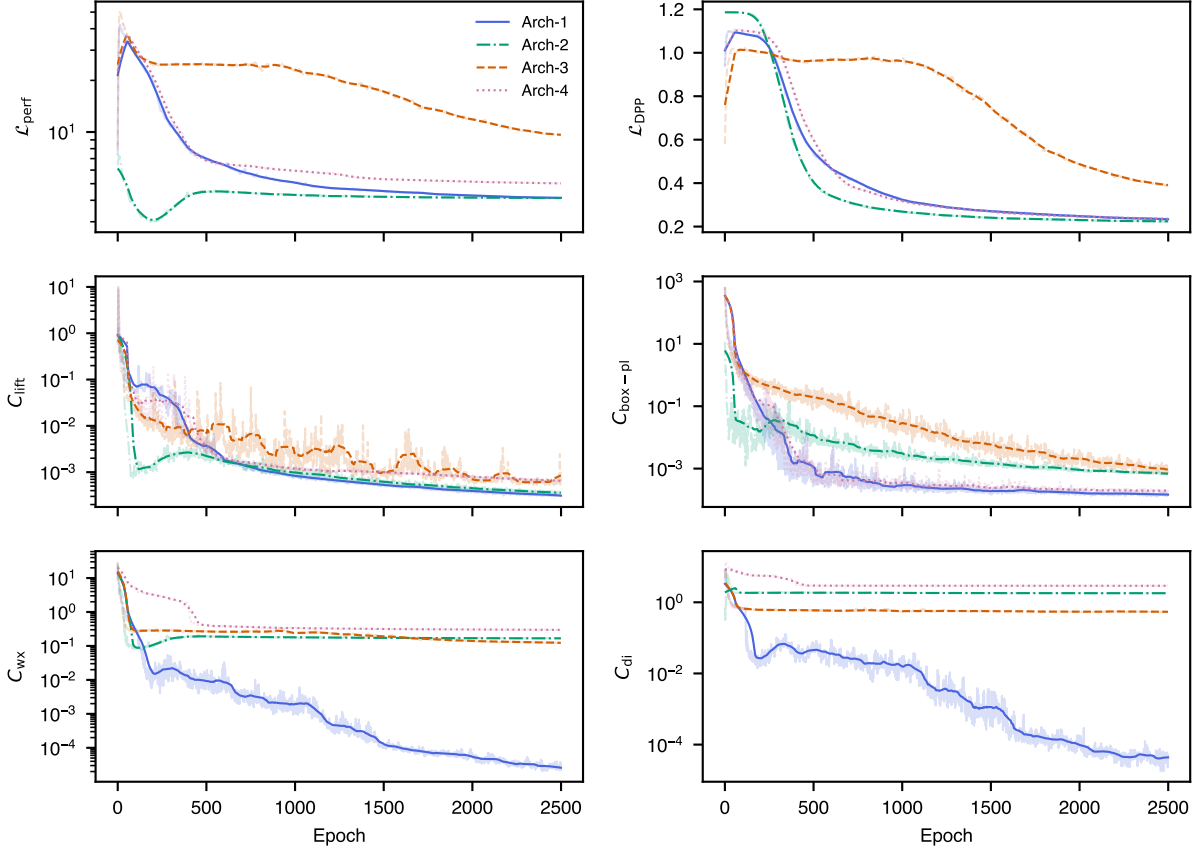


Figure C.18: DF-GLUE training losses over 2500 epochs for Architectures 1–4 (10 seeds, mean only).

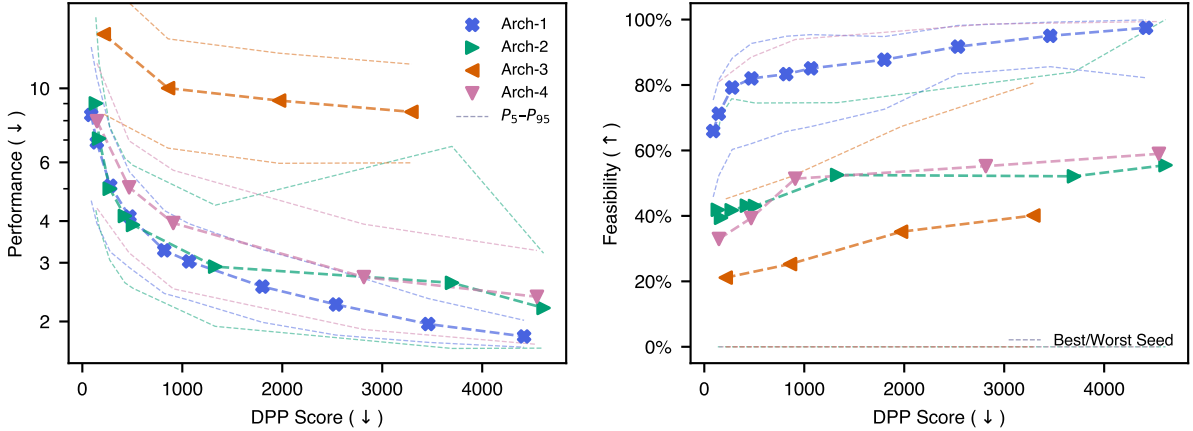


Figure C.19: Feasibility and performance–diversity trade-off across Architectures 1–4 (10 seeds): Architecture 1 achieves consistently high feasibility and the best trade-off, Architecture 3 degrades both feasibility and performance most strongly, and Architecture 4 attains best-seed feasibility similar to Architecture 1 but with much poorer mean robustness.

Appendix C.2.2. Discussion

Architecture 2. Architecture 2 removes the custom initialization and therefore starts with substantially lower output variance. As a result, early training exhibits low diversity in \mathcal{Z} , *i.e.*, designs are practically mode-collapsed at training epoch 0. For the seeds that fail to learn the wing placement constraints (C_{wx} and C_{di}), we observe that the corresponding head outputs at initialization are clustered at the saturation limits of the tanh or sigmoid nonlinearities. In this regime, gradients through the output acti-

vations are strongly attenuated, which impairs corrective updates and can prevent the optimizer from moving the outputs back into a high-gradient region. This explains the reduced robustness of Architecture 2. Convergence is not uniformly worse, but a subset of seeds becomes trapped by activation saturation and the resulting vanishing-gradient bottleneck. Low output variance increases sensitivity to small stochastic differences across runs, as without significant output variance the whole training batch can be in a vanishing gradient regime.

Architecture 3. Architecture 3 shifts capacity from the shared main block into the fuselage and wing latent heads. While this increases expressivity for predicting z_F , $z_{W,1}$, and $z_{W,2}$ from CF, it simultaneously reduces the capacity of the shared mapping $\zeta \mapsto \text{CF}$ that all other heads rely on. In effect, CF becomes closer to a shallow, near-linear (single nonlinearity due to one layer) lifting of the system-level latent ζ , rather than a rich intermediate representation that encodes higher-order interactions between subsystems.

This change particularly disadvantages heads that must condition on detailed wing and fuselage geometry to make compatible downstream decisions, such as wing placement and internals (latent and placement). In Architecture 1, these heads operate on CF that can reflect “nearly finalized” wing and fuselage implications. In Architecture 3, the reduced-capacity main block cannot reliably distill such information into CF, so the placement and internals heads are effectively asked to infer compatibility decisions from a representation that is close to the system-level latent ζ . Consequently, even if the wing/fuselage latent predictions themselves are expressive, the remaining subsystems receive an impoverished conditioning signal and cannot adapt their outputs to the realized wing and fuselage designs, which degrades constraint satisfaction and the overall performance–diversity trade-off.

Overall, Architecture 3 highlights that the shared main block must have sufficient capacity. It is not merely a routing module, but the primary mechanism that converts the system-level latent into a globally informative CF representation that supports coordination across heterogeneous heads.

More broadly, this ablation also raises a question about what information the system-level latent ζ is expected to carry under our training setup. We view this as an interesting direction for future work. In principle, one might hope that ζ alone is sufficiently informative to support all downstream decisions (including detailed placement). However, Architecture 3 suggests that, in practice, predicting high-quality placement and internals may require an intermediate representation (CF) that is *more information-dense and interaction-aware* than a shallow lifting of ζ . A key question is whether ζ should be trained to be directly usable for all subsystem placement and constraint satisfaction, or whether it is preferable for ζ to remain a compact global representation that is intentionally refined into task-specific coordination features by the main block.

Architecture 4. For Architecture 4, we also observe failures that are consistent with vanishing gradients. A plausible explanation is the reduced number of skip connections in the deep sequential wing placement head. However, our diagnostics indicate that the vanishing gradients also occur at the final output linear layer, directly before the bounded tanh / σ activation and subsequent denormalization. This makes depth (without adequate skip connections) an unlikely root cause for gradient vanishing, since one might expect vanishing gradients to only appear earlier in the stack if depth alone were the primary driver.

We therefore cannot conclusively attribute the robustness degradation in architecture 4 to the reduced skip-connection structure. Another possibility is that the custom initialization

is not applied as intended for this architecture (e.g., due to differences in module structure), which could change early pre-activation magnitudes and increase the likelihood of output saturation. However, despite careful checks and repeated attempts to match initialization behavior, we were not able to make Architecture 4 converge as robustly as Architecture 1.

Appendix C.2.3. Recommendations and Future Work

Our main recommendation from this ablation is to avoid sigmoid and tanh at head outputs where possible, since saturation leads to vanishing gradients and can strongly reduce robustness across seeds.

More broadly, the sensitivity of DF-GLUE’s ability to learn constraints and optimize performance to its architecture appears to be driven mostly by classical neural-network training issues rather than fundamental roadblocks. We hypothesize that with a better choice of output activations and sufficient skip connections to preserve gradient flow, the dominant remaining architecture choice is how to distribute capacity between the shared main block and the output heads as discussed relating to architecture 3.

Furthermore, future work for DF-GLUE should investigate state-of-the-art architectures beyond our simple MLP (e.g., graph-based networks, diffusion, Transformers, ...) and output parameterizations that train robustly and generalize across different problem settings without manual tuning.

Appendix D. Adaptive Augmented Lagrangian Update Schemes

Algorithm 2 Hypercube Adaptive Augmented Lagrangian Method

Require: Constraint violations $\mathbf{c}_t \in \mathbb{R}^{B \times K}$ at epoch t
Require: ALM parameters $\alpha, \gamma, \varepsilon$, warmup epochs T_{warmup}
1: **Input:** Current state variables $\mathbf{v}_{t-1}, \boldsymbol{\mu}_{t-1}, \boldsymbol{\lambda}_{t-1} \in \mathbb{R}^{B \times K}$
2: $\mathbf{c}_t = c_{\text{cap}} \cdot \tanh(\mathbf{c}_t / c_{\text{cap}})$ ▷ Smooth cap on \mathbf{c}_t
3: $\mathbf{c}_t^2 \leftarrow \mathbf{c}_t \odot \mathbf{c}_t$ ▷ Element-wise square
4: $\mathbf{v}_t \leftarrow \alpha \mathbf{v}_{t-1} + (1 - \alpha) \mathbf{c}_t^2$
5: $s \leftarrow \min(1, t / T_{\text{warmup}})$ ▷ Warmup ramp
6: $\Delta \boldsymbol{\mu}_t \leftarrow \gamma \cdot s \cdot \frac{|\mathbf{c}_t|}{\sqrt{\mathbf{v}_t} + \varepsilon}$ ▷ Adaptive penalty increment
7: $\boldsymbol{\mu}_t \leftarrow \boldsymbol{\mu}_{t-1} + \max(0, \Delta \boldsymbol{\mu}_t)$ ▷ Non-negative penalty parameters
8: $\boldsymbol{\lambda}_t \leftarrow \boldsymbol{\lambda}_{t-1} + \boldsymbol{\mu}_t \odot \mathbf{c}_t$ ▷ Lagrange multiplier update
9: **Return:** Updated weights $\boldsymbol{\lambda}_t$

Here, B denotes the batch size (number of hypercube volumes), K represents the number of constraints, and \odot denotes element-wise multiplication. The warmup epochs T_{warmup} enable a gradual ramp-up of the penalty parameters $\boldsymbol{\mu}_t$ during early training. This gradual increase is necessary to avoid overly aggressive constraint satisfaction, which ensures better early-training stability.

The key difference between pooled and hypercube schemes lies in how they handle constraint violations across the batch. The pooled approach takes the mean across all batch elements for each constraint, while the hypercube approach accounts for

potentially poor scaling of constraint violations across different designs. For example, a constraint could be poorly normalized and exhibit much larger values for bigger aircraft or at specific design points, which could skew penalty growth in the pooled approach. The hypercube scheme maintains separate tracking of distinct zones in \mathcal{Z} , with each zone having its own weight set for every constraint. Importantly, the hypercube approach only works because we consistently sample each batch element from the same hypercube region in ζ across training. In contrast, the pooled approach is more flexible and works with other sampling methods, such as $\zeta \sim \mathcal{N}$ or $\zeta \sim \mathcal{U}$.

Algorithm 3 Pooled Adaptive Augmented Lagrangian Method

Require: Constraint violations $\mathbf{c}_t \in \mathbb{R}^{B \times K}$ at epoch t
Require: ALM parameters $\alpha, \gamma, \varepsilon$, warmup epochs T_{warmup}

- 1: **Input:** Current state variables $\mathbf{v}_{t-1}, \boldsymbol{\mu}_{t-1}, \boldsymbol{\lambda}_{t-1} \in \mathbb{R}^{1 \times K}$
- 2: $\bar{\mathbf{c}}_t \leftarrow \frac{1}{B} \sum_{i=1}^B \mathbf{c}_{t,i}$ ▷ Pool constraints across batch
- 3: $\mathbf{c}_t \leftarrow \text{repeat}(\bar{\mathbf{c}}_t, B)$ ▷ Broadcast to all samples
- 4: $\mathbf{c}_t = c_{\text{cap}} \cdot \tanh(\mathbf{c}_t / c_{\text{cap}})$ ▷ Smooth cap on \mathbf{c}_t
- 5: $\mathbf{c}_t^2 \leftarrow \mathbf{c}_t \odot \mathbf{c}_t$ ▷ Element-wise square
- 6: $\mathbf{v}_t \leftarrow \alpha \mathbf{v}_{t-1} + (1 - \alpha) \mathbf{c}_t^2$
- 7: $s \leftarrow \min(1, t/T_{\text{warmup}})$ ▷ Warmup ramp
- 8: $\Delta\boldsymbol{\mu}_t \leftarrow \gamma \cdot s \cdot \frac{|\mathbf{c}_t|}{\sqrt{\mathbf{v}_t} + \varepsilon}$ ▷ Adaptive penalty increment
- 9: $\boldsymbol{\mu}_t \leftarrow \boldsymbol{\mu}_{t-1} + \max(0, \Delta\boldsymbol{\mu}_t)$ ▷ Non-negative penalty parameters
- 10: $\boldsymbol{\lambda}_t \leftarrow \boldsymbol{\lambda}_{t-1} + \boldsymbol{\mu}_t \odot \mathbf{c}_t$ ▷ Lagrange multiplier update
- 11: **Return:** Updated weights $\boldsymbol{\lambda}_t$ for constraint penalties

Table D.7 demonstrates that the ALM dual growth rate γ has a direct effect on the trade-off between constraint satisfaction, optimality, and diversity. Generally, a higher growth rate γ leads to better feasibility, as constraint satisfaction is weighted more heavily, but at the expense of worse optimality and diversity. For all GLUE model training in this work, we use $c_{\text{cap}} = 5.0$ and $\gamma = 5 \times 10^{-3}$.

Appendix E. Details on UAV Design Problem

Single-objective optimization (lowest mass given conditions) is performed. The conditions, which are fixed, are:

- Velocity and altitude: Affect drag and wing lift, and thus affect wing geometry
- Payload mass: simulates internal subsystems like radars, battery, and cargo. Essentially, we fix masses for internal boxes which the aircraft must accommodate.
- Payload box volumes: Additionally, we prescribe volumes for internal boxes which the aircraft must accommodate.

For more details on the specific test cases and experimental conditions, refer to Appendix G. Drag estimation is also implemented in the geometry layer, but due to scoping we focus only on the mass objective. Drag optimization also tends to promote high-aspect-ratio configurations that complicate visualization and analysis. Issues considering stability or dynamic aircraft

performance are entirely ignored. For this reason, the lift requirement for the rear wing $L_{\text{req},2}$ is set to $1/5 \cdot L_{\text{req},1}$. Only level flight performance is considered.

Experiments are run at three different sets of velocity, altitude, cargo mass, and volume. See Appendix G for more details.

Appendix E.1. Dimensionality of Design Spaces

Provided here is a detailed breakdown of the dimensionalities for the latent space \mathcal{Z} , design space \mathcal{X} , conditions c , and system-level latent space ζ used in the aircraft design problem.

Additional notes:

- **Wing geometry** (x_W): Each wing is parameterized by angle of attack (AoA), 64 airfoil points (x,z coordinates = 128 values), span, and chord, totaling 131 dimensions per wing. With 2 wings: $2 \times 131 = 262$ dimensions.
- **Internals geometry** (x_I): Three bounding boxes are placed inside the fuselage. Each box requires Two-Dimensional (2D) position (x,z) since $y=0$ for each bounding boxes' center, and Three-Dimensional (3D) dimensions (length, width, height). Total: $3 \times (2 + 3) = 15$ dimensions. The first box is fixed in space, removing 2 degrees of freedom: $15 - 2 = 13$ dimensions.
- **Coupling variables** (x_C): Lift requirements $l_{1,\text{req}}$ and $l_{2,\text{req}}$ are used as conditions during wing model inference rather than direct geometry instantiation, but are still counted in \mathcal{X} . Placement variables determine spatial relationships between subsystems.
- **Dimensionality reduction**: The subsystem models compress from $\text{dim}(\mathcal{X}) = 324$ to $\text{dim}(\mathcal{Z}) = 2$, a reduction factor of $14.7\times$.
- **System-level latent space** (ζ): For visualization purposes (latent space sweeps), $\text{dim}(\zeta) = 2$ is used. For all other experiments, $\text{dim}(\zeta) = 4$ is used.

Appendix E.2. Constrained Optimization Problem

For our UAV design problem, we have $n_o = 1$ (mass minimization) and $n_c = 5$. Of the five constraints, three are equality constraints for wing positioning and lift, and two are inequality constraints for wing-fuselage and internals-fuselage interfacing. The geometry layer outputs:

$$\mathcal{G}(\mathbf{x}) = [O_{\text{mass}}(\mathbf{x}), C_{\text{lift}}(\mathbf{x}), C_{\text{wx}}(\mathbf{x}), C_{\text{di}}(\mathbf{x}), C_{\text{bb}}(\mathbf{x}), C_{\text{box-pl}}(\mathbf{x})] \quad (\text{E.1})$$

where O_{mass} is the mass objective (to be minimized), C_{lift} is the lift constraint, C_{wx} represents wing placement constraints, C_{di} are dihedral constraints, C_{bb} is the bounding box constraint, and $C_{\text{box-pl}}$ is the box placement constraint. These are detailed in Section Appendix E.2.2.

Table D.7: Comparison of performance, diversity and feasibility at various hyperparameters γ and c_{cap} for DF-GLUE training with case 1.

γ (ALM)	c_{cap}	O_{mass}	Feasible	DPP($x, \sigma=0.5$)	DPP($z_F, \sigma=0.05$)
5×10^{-2}	5	4.34	75.6%	3647	213
5×10^{-3}	5	4.21	61.0%	3597	190
5×10^{-4}	5	4.07	42.7%	3558	187
5×10^{-2}	20	4.32	75.2%	3633	155
5×10^{-3}	20	4.21	59.7%	3577	133

Table E.8: Dimensionality breakdown for aircraft design problem

Subsystem Latents \mathcal{Z}	
z_W (Wing)	2x2
z_I (Internals)	4
z_F (Fuselage)	4
x_C (Coupling vars)	
Wing lift requirement	2x1
Wing 1 placement	2
Wing 2 placement	4
Internals placement	2
Total dim(\mathcal{Z})	22
GLUE Model Conditions c	
Box volumes	3
Cargo mass	1
Altitude	1
Velocity	1
Total dim(c)	6
Design Space \mathcal{X}	
x_F (Fuselage)	39
x_W (Per wing)	2x131
x_I (Internals)	13
x_C (Coupling)	10
Total dim(\mathcal{X})	324
System-level Latent ζ	2-4

The formal optimization problem is:

$$\min_{\mathbf{z} \in \mathcal{Z}} O_{\text{mass}}(\mathbf{x}(\mathbf{z})) \quad (\text{E.2})$$

$$\text{subject to } C_{\text{lift}}(\mathbf{x}(\mathbf{z})) = 0 \quad (\text{E.3})$$

$$C_{\text{wx}}(\mathbf{x}(\mathbf{z})) = 0 \quad (\text{E.4})$$

$$C_{\text{di}}(\mathbf{x}(\mathbf{z})) = 0 \quad (\text{E.5})$$

$$C_{\text{bb}}(\mathbf{x}(\mathbf{z})) \leq 0 \quad (\text{E.6})$$

$$C_{\text{box-pl}}(\mathbf{x}(\mathbf{z})) \leq 0 \quad (\text{E.7})$$

$$\mathbf{z} \in \mathcal{Z}$$

where $\mathbf{x}(\mathbf{z}) = \{\mathcal{S}_i(z_i)\}_i \cup \{x_C\}$ represents the complete design parameters obtained from subsystem latent codes via their respective generative models and the coupling variables.

Appendix E.2.1. Heuristics-Based Objective Function

The mass objective O_{mass} (Eq. E.2) is formulated as:

$$O_{\text{mass}}(\mathbf{x}) \propto m_{\text{wing}}(\mathbf{x}) + m_{\text{fuselage}}(\mathbf{x}) \quad (\text{E.8})$$

where:

$$m_{\text{wing}}(\mathbf{x}) \propto \alpha_w \cdot (\text{span}_1^2 \cdot \text{chord}_1 + \text{span}_2^2 \cdot \text{chord}_2) \quad (\text{E.9})$$

$$m_{\text{fuselage}}(\mathbf{x}) \propto \alpha_f \cdot A_{\text{surface, fus}} \quad (\text{E.10})$$

The wing mass scales with the square of span times chord (accounting for bending moment), while fuselage mass is proportional to surface area. Here α_w and α_f are scaling constants. Note that these mass formulations are heuristic approximations rather than high-fidelity structural analyses. In the future, these heuristics could be replaced with high-fidelity differentiable surrogates or simulators for more accurate performance predictions.

Appendix E.2.2. Constraint Formulations

Lift Constraint (C_{lift}). Ensures adequate lift generation:

$$C_{\text{lift}} \propto \frac{L_{\text{required}} - L_{\text{supplied}}}{L_{\text{required}}} \quad (\text{E.11})$$

where $L_{\text{required}} = g(m_{\text{wing}} + m_{\text{fuselage}} + m_{\text{cargo}})$ and $L_{\text{supplied}} = L_1 + L_2$ where L_1 is the lift of the front wing, and L_2 is the lift of the rear wing.

Wing Placement Constraints (C_{wx}). Ensure wing base positions match fuselage interface:

$$C_{\text{wx}} \propto C_{\text{wx},1} + C_{\text{wx},2} \quad (\text{E.12})$$

where:

$$C_{\text{wx},1} \propto |y_{w1} - y_{\text{PS1}}| \quad (\text{E.13})$$

$$C_{\text{wx},2} \propto \sqrt{(x_{w2} - x_{\text{PS2}})^2 + (y_{w2} - y_{\text{PS2}})^2 + (z_{w2} - z_{\text{PS2}})^2} \quad (\text{E.14})$$

Here, PS denotes the primary segments of the fuselage parametrization (see Figure B.13), whose planar faces define the wing base attachment points. Wing 1 (w1) is constrained in the y-coordinate only (spanwise position), as the primary segment 1 x and z positions are fixed anchors for the entire aircraft (origin of coordinate system). Wing 2 (w2) requires full 3D position matching.

Dihedral Constraints (C_{di}). Ensure wing orientations match fuselage interface:

$$C_{\text{di}} \propto \sum_{i=1}^2 |\Gamma_{\text{wing},i} - \Gamma_{\text{fuselage},i}| \quad (\text{E.15})$$

For the sake of simplicity, the wing orientation is only defined by the dihedral angle $\Gamma_{\text{wing},i}$. The wing's two remaining degree of freedom are sweep (fixed) and the angle of attack, which is handled by airfoil generation (BézierGAN).

Bounding Box Constraints (C_{bb}). Ensure wing roots fit within bounding box interface:

$$C_{\text{bb}} \propto \sum_{i=1}^2 \left[\max(0, a_{\text{wing},i} - a_{\text{fuselage},i}) + \max(0, b_{\text{wing},i} - b_{\text{fuselage},i}) \right] \leq 0 \quad (\text{E.16})$$

where (a_i, b_i) are the bounding box dimensions at wing-fuselage interface i . Note that b_i is effectively the extrusion length of the primary segment.

Box Placement Constraints ($C_{\text{box-pl}}$). Ensure internal components fit inside fuselage:

$$C_{\text{box-pl}} \propto \sum_{j=1}^{N_{\text{boxes}}} \sum_{k=1}^8 \max(0, -d_{j,k} - \delta) \leq 0 \quad (\text{E.17})$$

where $d_{j,k} = d(\mathbf{p}_{j,k}, \partial\Omega_{\text{fuselage}})$ is the signed distance from corner k of box j to the fuselage surface, and δ is a safety margin.

All constraints and objectives are normalized with conditions and scaled by a constant factor to ensure they are of similar magnitude.

Appendix F. DPP Loss Implementation

This appendix details the DPP loss implementation used here, both for training of models and diversity measurements. The DPP loss encourages diversity in generated aircraft designs by penalizing similarity between samples in a batch, building on the foundational work of Elfeki *et al.* [46].

Appendix F.1. Experimental Details

Table F.9 summarizes the settings used for the different experiments.

Table F.9: DPP settings for the different experiments. The domain indicates which feature space the DPP loss is applied to. \mathcal{X}_{vis} = Visually important features in \mathcal{X} (chord, span, main fuselage parameters).

Experiment	Kernel σ	Domain
Opt-Feas-Div (Fig. 6)	0.5	\mathcal{X}
Opt-Feas-Compute (Fig. 7)	-	-
SN Ablation (Tab. 3)	0.5	\mathcal{X}_{vis}
Mode Collapse Abl. (Tab. 4)	0.05	\mathcal{Z}

DPP scoring also depends on batch size. In benchmarking, we thus fix 35 samples for all evaluations and repeat the computation 20 times with different random batches, ensuring statistically consistent, method-agnostic comparison for very large sample sets.

Appendix F.2. Formulation

The DPP loss is based on the log-determinant of a similarity kernel matrix:

$$\mathcal{L}_{\text{DPP}} = -\log \det(\mathbf{K} + \epsilon \mathbf{I}) \quad (\text{F.1})$$

where \mathbf{K} is the similarity kernel matrix, ϵ is a regularization parameter, and \mathbf{I} is the identity matrix.

The similarity kernel is computed using a Gaussian radial basis function:

$$K_{ij} = \exp\left(-\frac{d^2(\mathbf{x}_i, \mathbf{x}_j)}{2\sigma^2}\right) \quad (\text{F.2})$$

where $d(\mathbf{x}_i, \mathbf{x}_j)$ is the Euclidean distance between samples i and j , and σ is the characteristic length scale.

Algorithm 4 DPP Loss Computation for GLUE Model Training

- 1: **Input:** $\mathbf{X} \in \mathbb{R}^{B \times D}$ (batch of B samples with D features), σ , ϵ
- 2: **Output:** \mathcal{L}_{DPP}
- 3: Compute pairwise squared distances: $\mathbf{D}^2 = \text{cdist}(\mathbf{X}, \mathbf{X})^2$
- 4: Compute similarity kernel: $\mathbf{K} = \exp(-\mathbf{D}^2/(2\sigma^2))$
- 5: Add regularization: $\mathbf{L} = \mathbf{K} + \epsilon \mathbf{I}$
- 6: Compute log-determinant: $\text{sign}, \log |\det(\mathbf{L})| = \text{slogdet}(\mathbf{L})$
- 7: Return: $\mathcal{L}_{\text{DPP}} = -2 \cdot \log |\det(\mathbf{L})|$

Shown in Algorithm 4 is the implementation used for training of DF-GLUE and benchmarking. It uses `torch.linalg.slogdet` for numerical stability to avoid overflow and underflow issues. The parameter σ can be varied to control the kernel length scale, where higher values of σ mean that samples farther away from each other will have greater influence on the diversity loss. The regularization parameter $\epsilon = 1 \times 10^{-2}$ prevents numerical issues with singular matrices.

In addition, for the training of some subsystem models, we use a slightly modified version of the DPP loss. The wing generator uses a performance-augmented DPP loss that incorporates aerodynamic quality metrics, following the approach of Chen and Ahmed [47]:

$$\mathcal{L}_{\text{PA-DPP}} = -\log \det(\mathbf{L}) \quad (\text{F.3})$$

where $\mathbf{L} = \mathbf{K} \odot (\mathbf{q}\mathbf{q}^T)$ and $q_i = \frac{(L/D_i)^2}{m_i^2}$ is the quality score for sample i .

The internals module employs three specialized DPP losses:

- Standard DPP: Z-score normalized diversity for box arrangements
- Aspect Ratio DPP: Diversity in box aspect ratios (width/length, height/length)
- Adjacency DPP: Diversity in spatial adjacency patterns between boxes

These variants use batch size normalization and robust Cholesky decomposition with eigenvalue fallback for numerical stability.

Appendix G. Overview of Test Cases for Aircraft Design Problem

Appendix H. Cross-Case Benchmarking

Table H.11 extends the analysis across three different aircraft design cases. Diversity measurements and sampling are identical to the analysis of case 1 above.

Table G.10: Comparison of mission and cargo requirements for the three optimization cases.

	Case 1	Case 2	Case 3
Velocity (m/s)	35	50	20
Altitude (m)	2000	2000	1000
Battery Mass (kg)	100	150	30
Electronics Mass (kg)	20	20	10
Payload Mass (kg)	30	30	20
Total Mass	150	200	60
Battery Volume (L)	45	75	15
Electronics Volume (L)	15	15	5
Payload Volume (L)	30	60	30
Total Volume	90	150	50

For case 1, the results are excerpts from Figure 6. Depending on hyperparameters, DF-GLUE can either reliably collapse to a highly optimal solution or exhibit the highest diversity among all methods. In terms of constraint satisfaction, the DF-GLUE model outperforms all data-driven GLUE models and is nearly competitive with the optimization algorithms (ALM-GD, TuRBO-iGD).

The same trend holds for cases 2 and 3. DF-GLUE consistently achieves higher feasibility than all data-driven approaches. While it does not quite match the precision with which the optimization algorithms can satisfy constraints, it remains close and clearly superior to purely DD-GLUE.

Regarding performance, the data-driven GLUE models tend to mimic the behavior of ALM-GD across all cases, suggesting they effectively learn similar design trade-offs. For case 3, TuRBO-iGD performs particularly poorly in terms of optimality. This further confirms our finding that TuRBO-iGD struggles with high-dimensional, constrained settings and is not well suited for our problem.

Note that the best objective of 0.87 reported for ALM-GD in case 3 appears anomalous. As of the time of writing, we are unsure what causes this.

Appendix I. Qualitative Comparison of Methods

Provided here is a visual comparison of samples obtained using optimization algorithms, data-driven GLUE models, and the data-free GLUE model.

- Bayesian optimization (TuRBO-iGD): Exhibits great diversity across configurations, but designs are generally speaking low-performance (large aircraft mass).
- ALM-GD: Finds better designs than Bayesian Optimization, but can struggle with local minima, as shown in several configurations. For example, when the internals model places component bounding boxes on top of each other rather than in a single row (which is beneficial for minimum fuselage diameter and thus weight), the fuselage cannot shrink (See second from the right in Figure I.20). In this case, there is a conflict between the box placement constraint (Eq. E.7, requiring boxes inside the fuselage) and the mass objective (Eq. E.2, favoring

smaller fuselage) which cannot be resolved. In other words, the optimizer is prone to get trapped in local minima.

- Data-driven GLUE Models: Since these models (cVAE, MDD-GAN, OT-GAN, DDPM) are trained on data acquired with ALM-GD, they tend to replicate similar designs to ALM-GD.
- Data-Free GLUE Model: Exhibits low diversity, with designs consistently in high-performance regions of the design space. Especially when trained without diversity losses, as shown here. In other words, the DF-GLUE robustly collapses to the global optimum if diversity is not explicitly incentivized. DF-GLUE does not produce *inherently* non-diverse designs. In fact, it can outperform optimization algorithms (I.) and data-driven models (II.) in terms of diversity if trained with large diversity loss weight λ_{DPP} .

Appendix J. Details on Optimization Algorithms

Table J.12 shows detailed hyperparameters for the optimization algorithms. For both methods, these are hand-tuned.

Appendix J.1. TuRBO-iGD

Bayesian optimization offers resilience against local minima and provides a valuable benchmark for global optimality. However, it suffers from poor scaling in high dimensions [74]. Our search space involves subsystem latent codes and coupling variables with $\text{dim}(\mathcal{Z}) = 22$. While specialized methods exist for high-dimensional BO [72, 73], they typically rely on pruning or embedding to compress the space. Since we already optimize in a compressed latent space, we estimate the marginal gain from these methods to be low. We therefore use TuRBO [74], which builds trust regions with lightweight GPs.

We find that the number of constraints poses an even greater challenge than dimensionality. We think this is because the feasible hypervolume shrinks multiplicatively with each additional constraint, especially for equality constraints with tight tolerances. For our five-constraint problem, standard TuRBO is effectively intractable. We address this by using an inner gradient descent (iGD) step for equality constraints with known convex structure (C_{wx} , C_{di} , C_{lift}), yielding TuRBO-iGD. This speeds up convergence because TuRBO only manages the feasibility of the remaining constraints, and the search dimensionality is reduced (22 to 15) as some variables are handled by iGD.

Figure J.21 illustrates the impact of this hybrid approach. Moving from two equality constraints handled by iGD (TuRBO-iGD2) to all three (TuRBO-iGD3) markedly improves convergence. Conversely, pure TuRBO without inner gradient descent rarely reaches feasibility.

To implement TuRBO-iGD, we decouple inequality constraints C_{box-pl} and C_{bb} , which are handled in the outer loop (TuRBO) from equality constraints (C_{lift} , C_{wx} , C_{di}) in the inner loop (iGD).

- *Outer Variables (\mathbf{x} , TuRBO):* Shape latents (z_w, z_F, z_I) and internals placement parameters x_I .

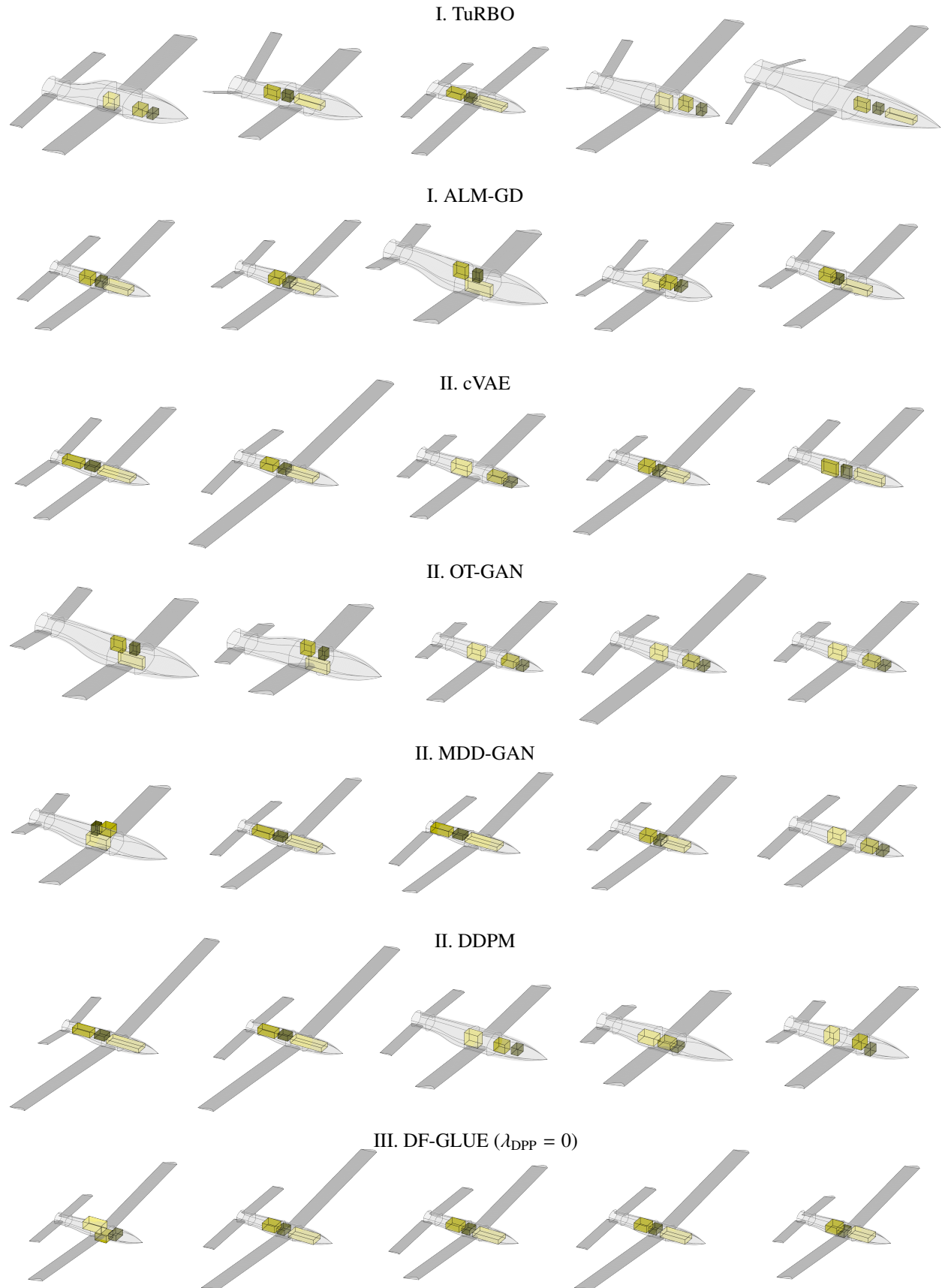


Figure I.20: Exemplar aircraft designs generated by all evaluated methods.

Table H.11: Comparison of optimality, feasibility, and diversity across conditions (see Appendix G).

Experiment	Samples	Seeds	Feas. (\uparrow)	Worst/Best Feas. (\uparrow)	Best Obj. (\downarrow)	Mean Obj. (\downarrow)	DPP (\downarrow)	
Case 1	TuRBO-iGD Top 1%	400	200	94.5%	-	1.89	4.23	1544
	ALM-GD 100%	70860	14180	97.2%	-	1.63	2.93	1424
	cVAE	10000	10	48.1%	(28.6% / 54.8%)	1.70	2.83	1689
	MDD-GAN 80%	10000	10	71.4%	(64.5% / 79.6%)	1.61	2.31	2301
	OT-GAN	10000	10	50.7%	(38.6% / 54.9%)	1.68	2.77	1886
	DDPM	10000	10	78.51%	(75.90% / 81.10%)	1.65	2.75	1460
	DF-GLUE λ_{perf} 0.05, λ_{DPP} 0.25	10000	10	85.9%	(70.7% / 94.6%)	1.80	3.33	986
Case 2	DF-GLUE λ_{perf} 0.05, λ_{DPP} 0.0	10000	10	96.5%	(73.5% / 99.7%)	1.63	1.90	4543
	TuRBO-iGD Top 1%	191	200	-	-	0.98	1.87	658
	ALM-GD 100%	47960	9592	92.6%	-	0.74	1.47	1375
	cVAE	10000	10	37.1%	(28.6% / 42.7%)	0.79	1.43	1568
	MDD-GAN 100%	10000	10	56.2%	(48.8% / 62.0%)	0.76	1.41	1551
	OT-GAN	10000	10	43.6%	(37.1% / 51.6%)	0.78	1.35	1740
	DDPM	10000	10	56.9%	(53.9% / 59.8%)	0.76	1.38	1439
Case 3	DF-GLUE λ_{perf} 0.1, λ_{DPP} 0.2	10000	10	78.0%	(0.0% / 98.6%)	0.67	1.37	1589
	TuRBO-iGD Top 1%	400	200	93.3%	-	16.32	35.98	1352
	ALM-GD 100%	64185	12837	94.0%	-	0.87	15.63	2609
	cVAE	10000	10	41.3%	(32.5% / 51.2%)	11.97	15.41	2955
	MDD-GAN	10000	10	62.9%	(45.5% / 70.8%)	11.74	14.75	3116
	OT-GAN	10000	10	50.9%	(44.5% / 59.1%)	11.85	15.51	2916
	DDPM	10000	10	54.1%	(47.8% / 57.8%)	11.94	14.12	2728
Case 4	DF-GLUE λ_{perf} 0.1, λ_{DPP} 0.75	10000	10	80.3%	(69.4% / 87.7%)	11.85	13.18	3158

Table J.12: Hyperparameters for optimization algorithms

ALM-GD		BayesOpt (TuRBO-iGD)	
Parameter	Value	Parameter	Value
Batch Size	5	Trust Regions (m)	5
Max Iterations	10 000	Max Iterations	8 000
Initial Sampling	Sobol	Initial Sampling	LHS
Primal Learning Rate (LR)	2.0e-3	Init. Points per Region	10
LR Decay	0.99	Acquisition Batch (q)	1
Dual LR (γ)	1.0e-2	Trust Region Length Min	0.5 ⁷
Constraint Cap	2.0	Trust Region Length Max	1.6
Gradient Clipping	Disabled	<i>Inner GD:</i>	
Patience (epochs)	50	Max Steps	8
Min. Improvement	0.02	Convergence Tol.	1.0e-4
Constraint Tolerance	1.0e-4		

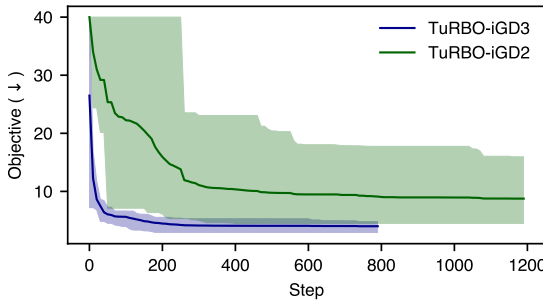


Figure J.21: Effect of inner gradient descent on convergence: TuRBO-iGD3 converges substantially faster than TuRBO-iGD2. Pure TuRBO rarely reaches feasibility.

- *Inner Variables (y , iGD):* Wing placement parameters $x_{W,pl}$ (position and dihedral angle) and lift requirements $L_{req,1}, L_{req,2}$.

Wing coordinates are reset to a fixed location before every iGD step regardless of fuselage shape. The solver must then position them to valid attachment points. We perform 8,000 iterations without auto-stopping, using on trust region restarts to escape local optima (as implemented by default in the TuRBO library).

The objective function f minimized by TuRBO (line 3 of Algorithm 5) combines the mass O_{mass} with soft penalties for the inequality constraints $C_{\text{box-pl}}$ and C_{bb} , which are not handled by the inner loop. We define $f = O_{\text{mass}} \cdot \psi(C_{\text{box-pl}}) \cdot \psi(C_{\text{bb}})$, where $\psi(C) = 1 + a_1 \tanh(C) + a_2 C$ imposes a steep penalty for violation. We use hand-tuned hyperparameters $a_1 = 5$ and $a_2 = 0.1$ in our experiments.

Algorithm 5 TuRBO-iGD Algorithm

```

Initialize TuRBO state and hyperparameters
while iterations < max iterations do
     $\mathbf{x} \leftarrow \text{TuRBO(GPs)}$  ▷ Sample candidate
    Initialize inner variables  $\mathbf{y}$ 
    repeat ▷ Enter inner loop
         $O_p, C_k \leftarrow \mathcal{G}(\mathbf{x}, \mathbf{y})$  ▷ Evaluate geometry
        Update  $\mathbf{y}$  via gradient descent on  $C_{\text{lift}}, C_{\text{di}}, C_{\text{wx}}$ 
    until  $C_{\text{lift}}, C_{\text{di}}, C_{\text{wx}} \leq \text{tol}$ 
     $f \leftarrow O_{\text{mass}} \cdot \psi(C_{\text{box-pl}}) \cdot \psi(C_{\text{bb}})$  ▷ Compute penalized
    objective
    Update GPs with  $(\mathbf{x}, f)$ 
end while

```

Appendix K. Details on Data-Driven GLUE Models

Appendix K.1. OT-GAN

The OT-GAN uses an entropic regularized optimal transport distance loss [22] implemented with the geomloss package [70]:

$$\mathcal{L}_{\text{OT}} = W_{\varepsilon}(G_{\theta}(\mathbf{z}), \mathbf{x}_{\text{real}}) \quad (\text{K.1})$$

where the blur parameter $\varepsilon(t)$ is annealed from $0.1 \rightarrow 0.02$ using a cosine schedule. Thanks to this, there is no adversarial training, only a Sinkhorn loss. The model uses only positive (feasible) training samples, with no negative data. We employ the 2-Wasserstein distance ($p = 2$). No DPP loss is used since training with optimal transport relieves GANs typical propensity to collapse to a single mode.

Appendix K.2. MDD-GAN

The MDD-GAN [45] distinguishes fake, feasible, and infeasible samples:

$$\begin{aligned} \mathcal{L}_D &= \mathcal{L}_{\text{CE}}(\mathbf{D}(G(\mathbf{z})), 0) \\ &+ \mathcal{L}_{\text{CE}}(\mathbf{D}(\mathbf{x}_{\text{valid}}), 1) \\ &+ \mathcal{L}_{\text{CE}}(\mathbf{D}(\mathbf{x}_{\text{invalid}}), 2) \end{aligned} \quad (\text{K.2})$$

$$\mathcal{L}_G = \mathcal{L}_{\text{CE}}(\mathbf{D}(G(\mathbf{z})), 1) + \lambda_{\text{div}} \cdot \mathcal{L}_{\text{DPP}}(G(\mathbf{z})) \quad (\text{K.3})$$

The model uses a three-way classification scheme, assigning label 0 to fake samples, label 1 to feasible samples, and label 2 to infeasible samples. To prevent mode collapse, we incorporate a DPP loss with weight $\lambda_{\text{div}} = 0.05$. This approach requires both positive and negative training samples.

Appendix K.3. cVAE

cVAE with binary feasibility labels:

$$\mathcal{L}_{\text{cVAE}} = \mathcal{L}_{\text{recon}} + \beta_{\text{KL}} \cdot \mathcal{L}_{\text{KL}} \quad (\text{K.4})$$

where $\mathcal{L}_{\text{recon}} = \mathbb{E}[\|\mathbf{x} - \hat{\mathbf{x}}\|_2^2]$ and $\mathcal{L}_{\text{KL}} = \mathbb{E}[-\frac{1}{2} \sum_i (1 + \log \sigma_i^2 - \mu_i^2 - \sigma_i^2)]$ with $\beta_{\text{KL}} = 0.3$. We augment the conditioning variables with a binary feasibility label such that $\mathbf{c}_{\text{aug}} = [\mathbf{c}, y]$ where $y \in \{0, 1\}$. The model employs the reparameterization trick $\mathbf{z} = \mu + \sigma \odot \epsilon$ where $\epsilon \sim \mathcal{N}(0, \mathbf{I})$ to enable backpropagation through the sampling process. At inference time, we only generate samples with the positive feasibility label ($y = 1$). Similar to MDD-GAN, this model requires both positive and negative training samples.

Appendix K.4. DDPM

The DDPM uses denoising diffusion with cosine noise schedule [25]:

$$\mathcal{L}_{\text{DDPM}} = \mathbb{E}_{t, \mathbf{x}_0, \epsilon} [\|\epsilon - \epsilon_{\theta}(\mathbf{x}_t, \mathbf{c}, t)\|_2^2] \quad (\text{K.5})$$

where $\mathbf{x}_t = \sqrt{\bar{\alpha}_t} \mathbf{x}_0 + \sqrt{1 - \bar{\alpha}_t} \epsilon$ with cosine schedule $\bar{\alpha}(t) = \cos^2\left(\frac{t/T+s}{1+s} \cdot \frac{\pi}{2}\right)$ and $s = 0.008$. The model uses a 128-dimensional sinusoidal time embedding to encode the diffusion timestep. We apply Exponential Moving Average (EMA) with rate $\gamma = 0.999$ to the model weights, which provides more stable sampling behavior. At inference time, the model applies 1000 denoising steps to generate samples. Unlike MDD-GAN and cVAE, this model uses only positive (feasible) training samples.

Appendix K.5. Model Capacity

All DD-GLUE models are based on fully connected architectures and are set up to use either deep MLP blocks (with skip connections every 6 layers) or wide residual blocks (WRBs) with configurable width multipliers. The latter are similar to those used in the DF-GLUE architecture, which is described in more detail in Appendix C. Based on hyperparameter optimizations, we find that the DDPM benefits from a wide residual block architecture. The DDPM thus uses 6 WRBs, which was found to be best during hyperparameter optimization. The cVAE, OT-GAN, and MDD-GAN use generic deep MLP blocks with skip connections every 6 layers. Table K.13 summarizes the feasibility scores (mean of two worst across four seeds per trial) obtained for each model and architecture choice during hyperparameter optimization.

Appendix K.6. Hyperparameters

Hyperparameter Optimization (HPO) is carried out for all data-driven GLUE models using the ax library [77] to ensure the relative difference in quality between the data-free and data-driven approach is not due to badly tuned hyperparameters. Table K.14 shows the hyperparameters for the data-driven GLUE models. Shown in bold are those hyperparameters optimized using HPO.

Appendix L. Differentiable Geometry Layer

This appendix provides technical details for the batched parametric geometry layer used in UAV design generation. It represents complete aircraft configurations through a modular, differentiable parametric representation comprising fuselage segments (cubic Bézier curves and bicubic Bézier surfaces, see Figure B.13), wings (scaled and extruded airfoil profiles), and internal payload boxes. The layer computes key metrics including frontal area, surface (wetted) area, and volume for fuselage drag and mass estimates, as well as wing induced drag. The mass estimate heuristically combines wing moments and fuselage surface area, while fuselage drag follows OpenVSP's Hoerner drag [78, 36]. Additionally, the layer performs validity checks for self-intersection, convexity, wing-fuselage interface quality, and containment of internal components ($C_{\text{box-pl}}$). These evaluations produce the outputs described in Equation E.1. The

Table K.13: Best robust feasibility scores (feasibility assessed as mean of 2 worst across 4 seeds per trial) obtained via HPO for different generative models and architectures.

Model	Architecture	HPO Trials	Seeds / Trial	Best Feasibility (↑)
cVAE	Deep MLP	40	4	48.63 %
cVAE	Wide ResBlocks	50	4	51.95 %
DDPM	Deep MLP	50	4	70.70 %
DDPM	Wide ResBlocks	50	4	77.34 %
MDD-GAN	Deep MLP	60	4	69.14 %
MDD-GAN	Wide ResBlocks	50	4	66.02 %
OT-GAN	Deep MLP	50	4	52.34 %
OT-GAN	Wide ResBlocks	50	4	49.22 %

Table K.14: Hyperparameters for data-driven generative models. Shown in bold are those hyperparameters optimized using Hyperparameter Optimization (HPO).

Parameter	OT-GAN	MDD-GAN	cVAE	DDPM
Architecture	Deep MLP	Deep MLP	Deep MLP	Wide Residual
Latent Dimension (d_z)	4	4	4	—
Hidden Dimension	620	620	280	512
Hidden Layers (G/Enc)	12	12	8	12
Hidden Layers (D/Dec)	—	12	8	—
Model Capacity (Params)	7M	14.8M	10.4M	54M + 54M EMA
<i>Breakdown</i>	—	G: 7M, D: 7.8M	E: 5.8M, D: 4.6M	—
Learning Rate (G/Model)	1.20e-4	5.50e-5	2.00e-4	4.50e-5
Learning Rate (D)	—	9.20e-5	—	—
Batch Size	1024	1024	1024	1024
Epochs	500	500	500	500
Noise Mode	Uniform	Uniform	Gaussian	Gaussian
Latent Scale	3.5	3.5	—	—
Augmentation Noise Scale σ_{aug}	5.80e-2	1.00e-2	2.00e-2	1.48e-1
Augmentation Sampling Factor N	5	8	5	10
KL Weight	—	—	0.3	—
Diversity Weight (λ_{div})	—	0.05	—	—
Time Embedding Dimension	—	—	—	128
Denoising Steps	—	—	—	1000
EMA Rate	—	—	—	0.999
Optimal Transport Blur (ε)	0.1 → 0.02	—	—	—
Discriminator Outputs	—	3	—	—

implementation enables *batch processing* while maintaining full differentiability for gradient-based optimization by treating discrete indexing operations as constants during backpropagation and using numerically stable formulations in PyTorch [71].

Appendix L.1. Overview

Figure L.22 shows the high-level overview of the differentiable geometry layer’s evaluation functionality. Some of these functions are used in the constraint checks and the objective function for DF-GLUE training and optimization algorithms. Others are used to train our subsystem models.

Appendix L.2. Fuselage Surface Area and Volume Computation

Computing geometric properties of parametric surfaces requires numerical integration. We employ adaptive tessellation where bicubic Bézier patches are uniformly sampled on an $(n \times n)$ grid in parameter space $(u, v) \in [0, 1]^2$. Each resulting quadrilateral cell’s area is approximated via the cross product of its edge vectors. Volume is computed by projecting these elements onto

the xz -plane and integrating, exploiting the fuselage’s bilateral symmetry about the xz -plane.

The bicubic Bézier surface is defined as:

$$\mathbf{B}(u, v) = \sum_{i=0}^3 \sum_{j=0}^3 B_i^3(u) B_j^3(v) \mathbf{P}_{ij} \quad (\text{L.1})$$

where $B_i^3(t)$ are cubic Bernstein polynomials and $\mathbf{P}_{ij} \in \mathbb{R}^{B \times 3}$ are control points for batch size B . In matrix form: $\mathbf{B}(u, v) = \mathbf{u}^T \mathbf{M} \mathbf{P}^T \mathbf{v}$, where \mathbf{M} is the Bézier basis matrix.

All operations are fully differentiable, utilizing only standard tensor operations (cross products, norms, summations). The method is vectorized across the batch dimension, enabling efficient parallel processing.

Implementation notes: Typical resolution is $n = 10$, yielding $(10-1)^2 = 81$ parallelogram elements per surface patch. The volume calculation projects each surface element onto the xz -plane by taking the y -component of the normal vector, then multiplies by the average y -coordinate of the element vertices. We only list the algorithm for bicubic area and volume computation here; for

```

AircraftBatch
├── .checkBoundingBoxSizeAgreement()
│   └── .BatchBezWing.getMinimalBoundingBoxDimensions()
│   └── .BatchFuselage.getBoundingBoxDimensions()
├── .checkWingPlacementAgreement() (accesses .fuselage.primary_segment*.wingbase_xyz)
├── .checkIfInternalsInsideSurface()
    └── .BatchInternals.getAllShiftedCornerPoints()
        └── .BatchBox.getCornerPoints()
    └── .checkIfPointInsideSurface()
        └── .BatchFuselage.checkIfInsideSurface()
            └── .BatchPrimarySegment.checkIfInsideSurface()
                └── .BatchBezierCurve.checkIfInsideCurve()
            └── .BatchBridgeSegment.checkIfInsideSurface()
                └── .BatchBezierSurface.checkIfInsideSurface()
            └── .BatchNoseTailSegment.checkIfInsideSurface()
                └── .BatchBezierSurface.checkIfInsideSurface()
├── .getLiftSupplied()
    └── .BatchBezWing.getNormalizedLift()
├── .getDrag()
    └── .BatchFuselage.getDrag()
        └── .getSurfaceAreaAndVolumeTesselation()
            └── .BatchPrimarySegment.getCrossSectionSurfaceAreaVolumeTesselation()
                └── .BatchBezierCurve.getArchLengthAndAreaOverSymmetryPlaneTesselation()
            └── .BatchBridgeSegment.getSurfaceAreaAndVolumeTesselation()
                └── .BatchBezierSurface.getSurfaceAreaAndVolumeTesselation()
            └── .BatchNoseTailSegment.getSurfaceAreaAndVolumeTesselation()
                └── .BatchBezierSurface.getSurfaceAreaAndVolumeTesselation()
        └── .getFrontalArea()
            └── .BatchPrimarySegment.getEquallySpaceYPoints()
                └── .BatchBezierCurve.getEquallySpacedYLocs()
    └── .BatchBezWing.getDrag()
        └── .BatchBezWing.getSurfaceArea()
├── .getMass()
    └── .BatchFuselage.getFirstOrderFuselageMass()
    └── .BatchBezWing.getMass()
    └── .BatchInternals.getBoxVolumes()
├── .checkSelfIntersection()
    └── .BatchFuselage.checkSelfIntersection()
        └── .BatchPrimarySegment.checkSelfIntersection()
            └── .BatchBezierCurve.checkSelfIntersection()
├── .evaluateConvexity()
    └── .BatchFuselage.evaluateConvexity()
        └── .BatchPrimarySegment.evaluateConvexity()
            └── .BatchBezierCurve.computeSignedCurvature()

```

Figure L.22: Differentiable geometry layer functionality overview.

the primary segments, which are extruded cubic Bézier curves, we apply essentially the same approach but in 1D—instead of 2D patches, we tessellate 1D line segments along the curve and compute cross-sectional properties accordingly.

Appendix L.3. Fuselage Frontal Area Computation

Frontal area (cross-sectional area in the yz -plane) is critical for drag estimation but cannot be computed via simple tessellation. The fuselage comprises multiple overlapping segments

(primary segments, bridge, nose), and we require the *outer envelope* formed by their union. Our approach: (1) determine vertical extent $[z_{\min}, z_{\max}]$ from segment control points, (2) generate N equally-spaced horizontal slices at z -coordinates \mathbf{z}_e , (3) interpolate y -coordinates along each segment’s Bézier curves at these z -values, (4) take the maximum y across all segments to obtain the outer envelope, and (5) integrate using the trapezoidal rule. For simplification, the current implementation approximates this envelope using only the primary fuselage segments.

Algorithm 6 Batched Surface Area and Volume Computation

Require: Bezier control points $\mathbf{P} \in \mathbb{R}^{B \times 4 \times 4 \times 3}$, tessellation resolution n

Ensure: Surface area $S \in \mathbb{R}^B$, volume $V \in \mathbb{R}^B$

- 1: $\mathbf{u}, \mathbf{v} \leftarrow \text{linspace}(0, 1, n)$ ▷ Parameter grid
- 2: Initialize $S \leftarrow 0_B, V \leftarrow 0_B$
- 3: **for** $i = 0$ to $n - 1$ **do**
- 4: **for** $j = 0$ to $n - 1$ **do**
- 5: $\mathbf{A} \leftarrow \text{BezierSurface}(\mathbf{P}, u_i, v_j)$ ▷ Shape: $[B, 3]$
- 6: $\mathbf{B} \leftarrow \text{BezierSurface}(\mathbf{P}, u_{i+1}, v_j)$
- 7: $\mathbf{C} \leftarrow \text{BezierSurface}(\mathbf{P}, u_i, v_{j+1})$
- 8: $\mathbf{d}_1 \leftarrow \mathbf{B} - \mathbf{A}, \mathbf{d}_2 \leftarrow \mathbf{C} - \mathbf{A}$ ▷ Edge vectors
- 9: $\mathbf{n} \leftarrow \mathbf{d}_1 \times \mathbf{d}_2$ ▷ Cross product in \mathbb{R}^3
- 10: $S += \|\mathbf{n}\|_2$ ▷ Accumulate parallelogram area
- 11: $V += |\mathbf{n}| \cdot \frac{|\mathbf{B}_y + \mathbf{C}_y|}{2}$ ▷ Volume via y-projection
- 12: **end for**
- 13: **end for** **return** S, V

The critical challenge is *differentiable interpolation*. Given query points \mathbf{z}_e not necessarily on the Bézier curve's natural parameterization $t \in [0, 1]$, we must invert the relationship $z = B_z(t)$ to find corresponding $y = B_y(t)$ values. We employ a two-stage approach: dense sampling of the Bézier curve followed by piecewise linear interpolation with careful gradient handling.

Algorithm 7 Batched Frontal Area Computation

Require: Primary segment Bezier curves $\{\mathbf{C}_k\}_{k=1}^K$, resolution N

Ensure: Frontal area $A_f \in \mathbb{R}^B$

- 1: $z_{\max} \leftarrow \max_k (\mathbf{C}_k^{\text{root}}, \mathbf{C}_k^{\text{bb-top}})$ ▷ Per-batch maximum $[B]$
- 2: $z_{\min} \leftarrow \min_k (\mathbf{C}_k^{\text{floor}}, \mathbf{C}_k^{\text{bb-bottom}})$ ▷ Per-batch minimum $[B]$
- 3: $\mathbf{w} \leftarrow \text{linspace}(0, 1, N)$
- 4: $\mathbf{z}_e \leftarrow z_{\min} \odot (1 - \mathbf{w}) + z_{\max} \odot \mathbf{w}$ ▷ Broadcast to $[B, N]$
- 5: **for** each segment $k \in \{1, \dots, K\}$ **do**
- 6: $\mathbf{y}_k \leftarrow \text{InterpolateBezier}(\mathbf{C}_k, \mathbf{z}_e)$ ▷ See Algorithm 3
- 7: **end for**
- 8: $\mathbf{y}_{\text{outer}} \leftarrow \max_k (\mathbf{y}_k)$ ▷ Outer envelope $[B, N]$
- 9: $\Delta z \leftarrow \mathbf{z}_e[:, 1 :] - \mathbf{z}_e[:, :-1]$ ▷ Slice heights $[B, N - 1]$
- 10: $\mathbf{y}_{\text{avg}} \leftarrow \frac{\mathbf{y}_{\text{outer}}[:, 1:] + \mathbf{y}_{\text{outer}}[:, :-1]}{2}$ ▷ Average widths
- 11: $A_f \leftarrow 2 \sum_{i=1}^{N-1} \Delta z_i \cdot \mathbf{y}_{\text{avg}, i}$ ▷ Factor 2 for symmetry **return** A_f

Gradient handling: The `searchsorted` operation is discrete. For backpropagation, the returned indices are treated as constants (zero gradient); gradients flow only through the values gathered and used in the subsequent linear interpolation. Small epsilon clamping ($\epsilon = 10^{-12}$) in the denominator prevents division by zero for perfectly horizontal curve segments while maintaining numerical stability. Typical parameters: $r = 50$, $N = 20$.

Appendix L.4. Ray-Casting Inside/Outside Test

Determining whether payload boxes violate the fuselage envelope requires testing potentially thousands of points simultaneously (for more complex subsystems with intricate geometries and many components; currently we use rectangular boxes with

Algorithm 8 Differentiable Bézier Curve Interpolation at Specified z -Coordinates

Require: Bezier curve \mathbf{C} , query z -coordinates $\mathbf{z}_e \in \mathbb{R}^{B \times N}$, sampling resolution r

Ensure: Interpolated y -coordinates $\mathbf{y}_e \in \mathbb{R}^{B \times N}$

- 1: $\mathbf{t} \leftarrow \text{linspace}(0, 1, r)$ ▷ Dense parameter sampling
- 2: $\mathbf{y}_c, \mathbf{z}_c \leftarrow \text{BezierCurve}(\mathbf{C}, \mathbf{t})$ ▷ Evaluate curve, shapes $[B, r]$
- 3: $\text{idx}_{\text{sort}} \leftarrow \text{argsort}(\mathbf{z}_c, \text{dim} = 1)$ ▷ Sort by z -coordinate
- 4: $\mathbf{z}_c \leftarrow \mathbf{z}_c[\text{idx}_{\text{sort}}], \mathbf{y}_c \leftarrow \mathbf{y}_c[\text{idx}_{\text{sort}}]$ ▷ Monotonic in z
- 5: $\text{idx}_r \leftarrow \text{searchsorted}(\mathbf{z}_c, \mathbf{z}_e)$ ▷ Binary search $[B, n]$
- 6: $\text{idx}_l \leftarrow \text{clamp}(\text{idx}_r - 1, 0, r - 2)$ ▷ Left bracket indices
- 7: $\text{idx}_r \leftarrow \text{clamp}(\text{idx}_r, 1, r - 1)$ ▷ Right bracket indices
- 8: $z_l, z_r \leftarrow \mathbf{z}_c[\text{idx}_l], \mathbf{z}_c[\text{idx}_r]$ ▷ Gather bracketing values
- 9: $y_l, y_r \leftarrow \mathbf{y}_c[\text{idx}_l], \mathbf{y}_c[\text{idx}_r]$
- 10: $t_{\text{lerp}} \leftarrow \frac{z_e - z_l}{\max(z_r - z_l, \epsilon)}$ ▷ $\epsilon = 10^{-12}$ prevents NaN gradients
- 11: $\mathbf{y}_e \leftarrow (1 - t_{\text{lerp}}) \odot y_l + t_{\text{lerp}} \odot y_r$ ▷ Linear interpolation
- 12: $\mathbf{y}_e \leftarrow \mathbf{y}_e \odot \mathbf{1}[0 \leq t_{\text{lerp}} \leq 1]$ ▷ Zero out-of-bounds queries
- 13: **return** \mathbf{y}_e

8 corner points each to test). We employ a vectorized ray-casting algorithm: for each query point \mathbf{p} , we cast a ray from a known interior origin \mathbf{o} to \mathbf{p} and compute the first intersection with the fuselage surface. If an intersection exists with parameter $t \in (0, 1]$, the signed distance indicates how far the point penetrates the surface.

The geometric problem reduces to solving the parametric intersection system:

$$\mathbf{o} + t\mathbf{d} = \mathbf{S}(u, v) \quad (\text{L.2})$$

where $\mathbf{d} = \mathbf{p} - \mathbf{o}$ is the ray direction, $\mathbf{S}(u, v)$ is a Bézier surface patch, and we seek (t, u, v) . For efficiency, we tessellate the surface into linear segments (reducing bicubic patches to piecewise bilinear approximations), yielding a series of 2×2 linear systems that can be solved in parallel.

For linearly extruded surfaces like primary segments, ray-casting is simplified to 2D intersection tests in the yz -plane (setting $x_0 = x_p$). For general bicubic surfaces (nose, bridge), we cast rays with a zero x -direction component but perform full 3D Möller-Trumbore intersection against the tessellated surface triangles.

Notation: Superscripts (1), (2) denote broadcasting dimensions for clarity. The `GetInteriorOrigin` function computes a guaranteed interior point by linearly interpolating between known segment boundaries at the query point's x -coordinate.

Gradient flow: The `argmax` on boolean masks is discrete. For backpropagation, the returned index is treated as a constant; gradients flow through the t value gathered at that index. Division-by-zero protection via small ϵ ensures bounded gradients.

Appendix L.5. Differentiable Box Overlap Detection

Training the autoregressive internal box generator requires a differentiable penalty for overlapping boxes. We compute pairwise overlapping volumes using the ReLU activation to smoothly handle non-overlapping cases (where overlap = 0).

Algorithm 9 Batched Ray-Casting Inside/Outside Test (2D Simplified View)

Require: Query points $\mathbf{P} \in \mathbb{R}^{B \times N \times 3}$, Bezier surface \mathbf{S} , resolution n

Ensure: Signed distances $\mathbf{d} \in \mathbb{R}^{B \times N}$ (positive = outside, 0 = on surface)

- 1: $\mathbf{O} \leftarrow \text{GetInteriorOrigin}(\mathbf{P})$ \triangleright Known-inside point $[B, N, 3]$
- 2: $\mathbf{a} \leftarrow \mathbf{P}_{yz} - \mathbf{O}_{yz}$ \triangleright Ray direction (YZ-plane only) $[B, N, 2]$
- 3: $\mathbf{u} \leftarrow \text{linspace}(0, 1, n)$ \triangleright Tessellation parameters
- 4: $\mathbf{A}, \mathbf{B} \leftarrow \text{TessellateSurface}(\mathbf{S}, \mathbf{u})$ $\triangleright [B, n-1, 3]$ endpoints
- 5: $\mathbf{c} \leftarrow \mathbf{B}_{yz} - \mathbf{A}_{yz}$ \triangleright Segment directions $[B, n-1, 2]$
- 6: $\mathbf{b} \leftarrow \mathbf{O}_{yz}^{(1)} - \mathbf{A}_{yz}^{(2)}$ \triangleright Broadcast to $[B, n-1, N, 2]$
- 7: $\triangleright \text{Solve: } \mathbf{O} + t\mathbf{a} = \mathbf{A} + s\mathbf{c}$ for (t, s) via Cramer's rule
- 8: $\text{den} \leftarrow \mathbf{a}_y^{(1)} \mathbf{c}_x^{(2)} - \mathbf{a}_x^{(1)} \mathbf{c}_y^{(2)}$ \triangleright Determinant $[B, n-1, N]$
- 9: $\text{num} \leftarrow \mathbf{a}_y^{(1)} \mathbf{b}_x - \mathbf{b}_y \mathbf{a}_x^{(1)}$
- 10: $s \leftarrow \begin{cases} \text{num}/(\text{den} + \epsilon) & |\text{den}| > \epsilon \\ -1 & \text{otherwise} \end{cases}$ $\triangleright \epsilon = 10^{-6}$
- 11: $\text{valid}_s \leftarrow (0 \leq s \leq 1) \wedge (|\text{den}| > \epsilon)$ \triangleright On segment?
- 12: $t \leftarrow \begin{cases} (\mathbf{c}_x^{(2)} s - \mathbf{b}_x)/(\mathbf{a}_x^{(1)} + \epsilon) & \text{valid}_s \\ 0 & \text{otherwise} \end{cases}$
- 13: $\text{valid} \leftarrow \text{valid}_s \wedge (t > 0)$ \triangleright Ray goes forward
- 14: $\text{idx}_{\text{first}} \leftarrow \text{argmax}_{\text{dim}=1}(\text{valid})$ \triangleright First valid intersection per ray
- 15: $t_{\text{hit}} \leftarrow t[\text{idx}_{\text{first}}]$ \triangleright Gather intersection parameters
- 16: $\text{has_hit} \leftarrow \text{any}_{\text{dim}=1}(\text{valid})$
- 17: $\mathbf{d} \leftarrow \|\mathbf{P} - \mathbf{O}\|_2 \odot (1 - t_{\text{hit}}) \odot \text{has_hit}$ \triangleright Signed distance

return \mathbf{d}

For axis-aligned boxes, two boxes overlap if and only if they overlap along all three axes. The overlap extent along each axis is given by:

$$\ell_\alpha = \max \left(0, \frac{d_{i,\alpha} + d_{j,\alpha}}{2} + \delta - |c_{i,\alpha} - c_{j,\alpha}| \right) \quad (\text{L.3})$$

where $d_{i,\alpha}$ is the dimension of box i along axis α , $c_{i,\alpha}$ is its center coordinate, and δ is a safety margin encouraging spacing. The total overlap volume is $O_{ij} = \ell_x \ell_y \ell_z$.

Algorithm 10 Differentiable Box Overlap Computation

Require: Box centers $\mathbf{c} \in \mathbb{R}^{B \times K \times 3}$, dimensions $\mathbf{d} \in \mathbb{R}^{B \times K \times 3}$, margin δ

Ensure: Overlap matrix $\mathbf{O} \in \mathbb{R}^{B \times K \times K}$

- 1: $\mathbf{c}_i \leftarrow \mathbf{c}[:, :, \text{None}, :]$ \triangleright Broadcast to $[B, K, 1, 3]$
- 2: $\mathbf{c}_j \leftarrow \mathbf{c}[:, \text{None}, :, :]$ \triangleright Broadcast to $[B, 1, K, 3]$
- 3: $\mathbf{d}_i, \mathbf{d}_j \leftarrow \text{analogous broadcasting}$
- 4: **for** $\alpha \in \{x, y, z\}$ (index 0, 1, 2) **do**
- 5: $\ell_\alpha \leftarrow \text{ReLU} \left(\frac{\mathbf{d}_{i,\alpha} + \mathbf{d}_{j,\alpha}}{2} + \delta - |\mathbf{c}_{i,\alpha} - \mathbf{c}_{j,\alpha}| \right)$
- 6: **end for**
- 7: $\mathbf{O} \leftarrow \ell_x \odot \ell_y \odot \ell_z$ \triangleright Element-wise product $[B, K, K]$
- 8: Set diagonal: $\mathbf{O}[:, i, i] \leftarrow 0$ for all i \triangleright Remove self-overlap

return \mathbf{O}

Appendix L.6. Payload Arrangement Convex Hull View Area

For volumetric efficiency scoring using in training of the box arrangement autoregressive model, we compute the convex hull of all internal box corners projected onto 2D views (frontal: yz , side: xz , top: xy). This provides a tight envelope of the usable internal volume. The challenge is implementing a 2D convex hull algorithm that is fully differentiable.

We employ a brute-force $O(n^3)$ approach based on the following geometric property: an edge (i, j) is on the convex hull if and only if all other points k lie on the same side of the line through i and j . This is tested via the cross product sign. Points identified as being on the hull are then sorted counter-clockwise by angle from their centroid, and area is computed via the shoelace formula.

Algorithm 11 Differentiable 2D Convex Hull Area

Require: 2D points $\mathbf{p} \in \mathbb{R}^{B \times N \times 2}$ (pre-sorted lexicographically, deduplicated)

Ensure: Convex hull area $A \in \mathbb{R}^B$

- 1: $\mathbf{p}_i \leftarrow \mathbf{p}[:, :, \text{None}, \text{None}, :]$ \triangleright Broadcast to $[B, N, 1, 1, 2]$
- 2: $\mathbf{p}_j \leftarrow \mathbf{p}[:, \text{None}, :, \text{None}, :]$ \triangleright Broadcast to $[B, 1, N, 1, 2]$
- 3: $\mathbf{p}_k \leftarrow \mathbf{p}[:, \text{None}, \text{None}, :, :]$ \triangleright Broadcast to $[B, 1, 1, N, 2]$
- 4: $\mathbf{v}_{ij} \leftarrow \mathbf{p}_j - \mathbf{p}_i$, $\mathbf{v}_{ik} \leftarrow \mathbf{p}_k - \mathbf{p}_i$
- 5: $\text{cross} \leftarrow \mathbf{v}_{ij,x} \mathbf{v}_{ik,y} - \mathbf{v}_{ij,y} \mathbf{v}_{ik,x}$ \triangleright 2D cross product $[B, N, N, N]$
- 6: $\text{all_geq} \leftarrow \text{all}_{\text{dim}=3}(\text{cross} \geq 0)$ \triangleright All points right of edge
- 7: $\text{all_leq} \leftarrow \text{all}_{\text{dim}=3}(\text{cross} \leq 0)$ \triangleright All points left of edge
- 8: $\text{edge}_{ij} \leftarrow \text{all_geq} \vee \text{all_leq}$ \triangleright Valid hull edge $[B, N, N]$
- 9: $\text{edge}[:, i, i] \leftarrow \text{False}$ for all i \triangleright Remove self-edges
- 10: $\text{on_hull}_i \leftarrow \text{any}_{\text{dim}=2}(\text{edge}_{ij})$ \triangleright Point on hull if any edge $[B, N]$
- 11: $n_h \leftarrow \sum_i \text{on_hull}_i$ \triangleright Hull size per batch element
- 12: $\mathbf{c} \leftarrow \frac{1}{\max(n_h, 1)} \sum_{i: \text{on_hull}_i} \mathbf{p}_i$ \triangleright Centroid $[B, 2]$
- 13: $\theta \leftarrow \text{atan2}(\mathbf{p}_y - \mathbf{c}_y, \mathbf{p}_x - \mathbf{c}_x)$ \triangleright Angles from centroid
- 14: $\theta[-\text{on_hull}] \leftarrow +\infty$ \triangleright Sort non-hull points to end
- 15: $\text{idx}_{\text{sort}} \leftarrow \text{argsort}(\theta, \text{dim} = 1)$ \triangleright Counter-clockwise order
- 16: $\mathbf{p}_{\text{hull}} \leftarrow \mathbf{p}[\text{idx}_{\text{sort}}]$ \triangleright Sorted hull points (padded)
- 17: \triangleright Shoelace formula with wrapping:
- 18: $\mathbf{x}, \mathbf{y} \leftarrow \mathbf{p}_{\text{hull}, x}, \mathbf{p}_{\text{hull}, y}$
- 19: $A \leftarrow \frac{1}{2} \left| \sum_{i=0}^{n_h-1} (x_i y_{(i+1) \bmod n_h} - x_{(i+1) \bmod n_h} y_i) \right|$ **return** A

Complexity and gradient handling: The `argsort` operation is discrete; gradients bypass the discrete operation and flow through the gathered point coordinates. Boolean operations (`all`, `any`) are treated as non-differentiable gates in the forward pass, with gradients flowing through the point coordinates in the backward pass. Variable hull sizes across the batch are handled via zero-padding and masking in the shoelace summation.

Relationship to frontal area: For internal boxes, the convex hull area in the yz -plane (frontal view) provides a lower bound on usable payload volume. This differs from fuselage frontal area (Algorithm 2), which computes the outer envelope for drag estimation.

Appendix L.7. Non-Differentiable Feasibility Checks

While the aforementioned methods are differentiable and used in training objectives, we also employ several discrete checks

for design validation and filtering.

Convexity via Curvature Analysis. To encourage smooth, manufacturable fuselage cross-sections, we check convexity of the primary segment Bézier curves. The signed curvature of a planar curve $\mathbf{B}(t) = [y(t), z(t)]$ is:

$$\kappa(t) = \frac{y'(t)z''(t) - y''(t)z'(t)}{(y'(t)^2 + z'(t)^2)^{3/2}} \quad (\text{L.4})$$

A perfectly convex curve has $\kappa(t)$ of constant sign. We sample κ at 50 uniformly spaced $t \in [0, 1]$ and count sign changes:

$$\text{ConvexityViolation} = \sum_{i=1}^{49} \mathbf{1}[\text{sign}(\kappa_i) \neq \text{sign}(\kappa_{i-1})] \quad (\text{L.5})$$

This metric is an integer and non-differentiable, but provides interpretable feedback. Designs with $\text{ConvexityViolation} > 0$ exhibit inflection points, which can lead to poor aerodynamic performance or manufacturing difficulties. This check is applied only to the primary fuselage segments, as bridge and nose segments inherently have controlled curvature variations.

Self-Intersection Detection. Self-intersecting Bézier curves are geometrically invalid. To detect self-intersection, we solve the algebraic system $\mathbf{B}(t_1) = \mathbf{B}(t_2)$ for $t_1 \neq t_2$. This is formulated as a small linear system derived from the curve's control points, which is then solved efficiently using normal equations (`torch.linalg.solve`). The solution yields candidate parameter pairs (t_1, t_2) which are then tested to ensure they fall within $[0, 1]$ and are distinct. This procedure is implemented using batch matrix operations but returns a boolean mask indicating self-intersection presence. It is used for post-hoc filtering rather than training objectives.